Starvation sensing by mycobacterial RelA/SpoT homologue through constitutive surveillance of translation

Yunlong Li[1#], Soneya Majumdar[2#], Ryan Treen[1,3#], Manjuli R. Sharma[2], Jamie Corro[1,3], Howard B. Gamper[4], Swati R. Manjari[2], Jerome Prusa[5], Nilesh K. Banavali[2], Christina L. Stallings[5], Ya-Ming Hou[4], Rajendra K. Agrawal[2,3*], Anil K. Ojha[1,3*]

1. Division of Genetics, Wadsworth Center, New York State Department of Health, Albany, NY 12208, USA

2. Division of Translational Medicine, Wadsworth Center, New York State Department of Health, Albany, NY 12237, USA

3. Department of Biomedical Sciences, School of Public Health, University at Albany, Albany, NY 12208, USA

4. Department of Biochemistry and Molecular Biology, Thomas Jefferson University, Philadelphia, PA 19107, USA

5. Department of Molecular Microbiology, Washington University in St. Louis School of Medicine, St. Louis, MO 63110, USA

[#]Equal contribution

*Correspondence: anil.ojha@health.ny.gov; rajendra.agrawal@health.ny.gov

Summary:

The stringent response, which leads to persistence of nutrient-starved mycobacteria, is induced by activation of RelA/SpoT homologue (Rsh) upon entry of a deacylated-tRNA in a translating ribosome. However, the mechanism by which Rsh finds such ribosomes *in vivo* remains unclear. Here we show that conditions inducing ribosome hibernation cause loss of intracellular Rsh in a Clp protease-dependent manner. The loss is also observed in non-starved cells when Rsh-ribosome interaction is abolished by mutation in Rsh, indicating that interaction with translating ribosomes is necessary for physiological stability of Rsh. The cryo-EM structure of the Rsh-bound 70S ribosome in a translation initiation complex reveals hitherto unknown interactions between the ACT domain of Rsh and components of the ribosomal L7/L12-stalk base, suggesting that the aminoacylation status of A-site tRNA is surveyed during the first cycle of elongation. Altogether, we propose a *surveillance model* of Rsh activation that originates from its constitutive interaction with translating ribosomes.

46 **Introduction:**

47 The stringent response in bacteria is a programmed adaption to nutrient starvation
48 facilitated by the secondary messengers, guanosine tetra- or penta-phosphates
49 [collectively called (p)ppGpp] (Cashel and Gallant, 1969; Chatterji and Ojha, 2001;
50 Potrykus and Cashel, 2008; Prusa et al., 2018). This adaptation mechanism promotes
51 long-term survival and persistence of mycobacteria under various stresses including
52 antibiotics (Dahl et al., 2003; Dutta et al., 2019; Richards et al., 2019; Stallings et al.,
53 2009; Vilcheze and Jacobs, 2019; Weiss and Stallings, 2013). The primary function of
54 (p)ppGpp is to reprogram the global gene expression in cells either directly by binding to
55 RNA polymerase (Potrykus and Cashel, 2008; Ross et al., 2013) or by binding to other
56 cellular targets (Dalebroux and Swanson, 2012; Diez et al., 2020; Irving et al., 2021).

57 The level of (p)ppGpp in *E. coli* is primarily regulated by a GDP/GTP
58 pyrophosphokinase encoded by RelA, and GDP/GTP pyrophosphohydrolase encoded
59 by SpoT (Potrykus and Cashel, 2008). Mycobacteria encode a single dual-function
60 enzyme, RelA/SpoT homologue (henceforth called Rsh), with both kinase and
61 hydrolase activities possessed by distinct domains of the enzyme (Avarbock et al.,
62 2005; Avarbock et al., 1999; Jain et al., 2006; Ojha et al., 2000; Primm et al., 2000). In
63 addition, mycobacterial Rsh also has a distinct C-terminal region with possible
64 autoinhibitory function, inferred from *in vitro* biochemical studies (Avarbock *et al.*, 2005;
65 Avarbock et al., 2000; Jain *et al.*, 2006), although occurrence of autoinhibition
66 mechanism *in vivo* is unknown. The optimum kinase activity of mycobacterial Rsh is
67 observed in a Rsh Activating Complex (RAC) comprising mRNA, deacylated-tRNA and

68 the ribosome (Avarbock *et al.*, 2000). Further insights into the domain architectures of
69 the enzyme and the mechanism of its activation can be derived from the structures of
70 free RelA from *Streptococcus dysgalactiae* (Hogg et al., 2004), or its *E. coli* and *B.*
71 *subtilis* homologues in complex with the ribosome, mRNA and A- and P-site tRNAs
72 (Arenz et al., 2016; Brown et al., 2016; Loveland et al., 2016). RelA has five distinct
73 domains (Fig. 1A): i) N-terminal domain possessing the (p)ppGpp synthase and
74 hydrolase activities, ii) TGS (ThrRS, GTPase, SpoT) domain that interacts with 3' CCA
75 tail of deacylated-tRNA, iii) alpha helical domain (AHD), iv) zinc-binding domain (ZBD)
76 that contacts the A-site finger (ASF) on the 23S rRNA and S19 at the inter-subunit
77 interface, and v) the ACT domain (Aspartate Kinase, Chorismate and TyrA) occupying a
78 cavity in the large 50S ribosomal subunit (or LSU) (Arenz *et al.*, 2016; Brown *et al.*,
79 2016; Loveland *et al.*, 2016). The interaction between the TGS domain and 3' CCA tail
80 of the deacylated-tRNA stabilizes the tRNA in the A/R state while pinning the domain
81 against the small 30S ribosomal subunit (or SSU) and extending the flexible catalytic N-
82 terminal of RelA in an open and active conformation (Arenz *et al.*, 2016; Brown *et al.*,
83 2016; Loveland *et al.*, 2016).
84 The mechanism by which RelA finds a stalled ribosome complex in a nutrient
85 starved cell remains unclear. According to a currently adopted 'hopping model',
86 diffusible RelA samples translation elongation complexes and binds to a stalled
87 ribosome with deacylated A-site tRNA in the A/R state, and upon catalyzing (p)ppGpp
88 synthesis the enzyme 'hops' to another stalled complex (Takada et al., 2021; Wendrich
89 et al., 2002; Winther et al., 2018). The hopping model further hypothesizes that an

90 inactive RelA in non-starved cells acquires a ribosome-free, closed conformation, in
91 which the catalytic activity is autoinhibited by the CTD, either through intermolecular
92 (Avarbock *et al.*, 2005; Gropp et al., 2001; Jain *et al.*, 2006) or intramolecular
93 interactions (Gratani et al., 2018; Mechold et al., 2002; Ronneau et al., 2019; Takada et
94 al., 2020; Tamman et al., 2020; Turnbull et al., 2019). Winther et al. later proposed that
95 free cytosolic RelA in *E. coli* binds to deacylated-tRNA before binding to the translating
96 ribosome (Winther *et al.*, 2018), although this model is challenged by: a) the evidence of
97 RelA bound to the ribosome without any A/R state tRNA (Loveland *et al.*, 2016), and b)
98 single-molecule tracking of RelA-fluorescent protein suggesting constitutive association
99 between RelA and ribosome in non-starved *E. coli* cells (English et al., 2011).
100 Recognizing these discrepancies, Takada et al. offered a refined hopping model in *B.*
101 *subtilis* in which activation of the stringent response appears to be initiated by a weak
102 interaction between Rsh and ribosome before the complex is stabilized by the entry of
103 deacylated-tRNA at the A-site, although they found RelA-ribosome interaction in *E. coli*
104 to be too weak to universally validate their model (Takada *et al.*, 2021). These studies
105 while revealing subtle differences in the properties of RelA/Rsh across bacterial
106 species, also underscore the limitations of biochemical assays in modeling a highly
107 dynamic *in vivo* interaction between the stringent factor and the translation machinery.
108 Besides the stringent response, nutrient starvation in bacteria also induces ribosome
109 hibernation, which is characterized by binding of a specialized protein near the decoding
110 center of the 70S ribosome to preserve the ribosome in an inactive and antibiotic
111 resistant state [reviewed in (Gohara and Yap, 2018; Li et al., 2021b; Prossliner et al.,

112 2018)]. *Mycobacterium smegmatis* and *Mycobacterium tuberculosis* (Mtb) induce
113 ribosome hibernation as a specific response to severe zinc starvation, a likely condition
114 in hosts during chronic TB infection (Lai et al., 2021; Li et al., 2020; Li et al., 2018).
115 Moderate zinc limitation also induces remodeling of ribosomes, in which ribosomal (r-)
116 proteins containing the CXXC motif (called C+ r- proteins) are replaced by their paralogs
117 without the motif (called C- r-proteins) (Li *et al.*, 2018; Prisic et al., 2015). The C-
118 ribosome is subsequently targeted for hibernation by mycobacterial protein Y (Mpy),
119 with assistance from a zinc-sensing protein called Mpy recruitment factor (Mrf) (Li *et al.*,
120 2020; Li *et al.*, 2018). A zinc-bound form of Mrf is sensitive to degradation by Clp
121 protease, such that Mrf accumulation increases with decreasing concentration of zinc
122 (Li *et al.*, 2020).
123 Investigating the interplay between the stringent response and ribosome hibernation
124 in mycobacteria, we show here that interaction with the ribosome is necessary for the
125 stability of intracellular Rsh in non-starved cells. The structure of Rsh-bound 70S
126 ribosome in a translation initiation complex allows us to propose a new mechanism of
127 starvation sensing by mycobacterial Rsh, in which its activation arises from its
128 engagement with translating ribosomes.
129
130 **Results:**
131 *Mrf attenuates the stringent response in zinc-starved mycobacteria*
132 We tested how a zinc limiting growth condition that induces ribosome hibernation in *M.*
133 *smegmatis* would impact ppGpp synthesis. After 96-hours of growth in high- or low-zinc

134 Sauton's medium, wildtype *M. smegmatis* cells were exposed for 3 hours to
135 macronutrient starvation in tris-buffered saline with Tween-80 (TBST) to induce the
136 stringent response to a measurable level (Stallings *et al.*, 2009). Rsh-dependent
137 accumulation of ppGpp upon TBST starvation of the high-zinc culture was significantly
138 greater than the low-zinc culture (Fig. 1B). To dissociate the contribution of
139 macronutrient depletion from zinc limitation in TBST, we examined the stringent
140 response in cells from high-zinc cultures after exposure to metal-chelated or zinc
141 supplemented TBST. Metal chelation did not impact the ppGpp synthesis, indicating
142 that macronutrient starvation in TBST was the primary inducer of the stringent response
143 (Fig. 1C).
144 Because interaction with ribosomes is critical for the stringent response, we
145 hypothesized that the attenuated stringent response in low-zinc cultures was likely due
146 to zinc-responsive changes in the ribosome structure and/or function. We therefore
147 analyzed the Rsh occupancy on the ribosome in high- and low-zinc cultures. Rsh
148 occupancy on the ribosomes purified from low-zinc cells was significantly lower than on
149 the ribosomes from high-zinc cells (Fig. 1D). Unexpectedly, the difference in Rsh
150 abundance on the ribosome tightly correlated with the levels in the total cellular lysate
151 (Fig. 1D). Moreover, lack of any other detectable antibody-recognizing Rsh isoforms
152 (Fig S1) suggests overall loss of intracellular Rsh. Together, figures 1B-D show that
153 physiological conditions developed during zinc starvation decreases the stability of Rsh
154 and its interaction with the ribosome, thereby diminishing the cellular potential to induce
155 the stringent response. Seeking further explanation, we investigated the effect of two

156 zinc-responsive physiological changes in the ribosome, remodeling and hibernation, in
157 altered Rsh stability and Rsh-ribosome interaction. The Zur-mediated C+ to C-
158 remodeling of the ribosome induced by zinc starvation did not impact the Rsh-ribosome
159 interaction: Rsh occupancy on the ribosome from a high-zinc culture of wildtype was
160 comparable to Δ*zur* and pYL53 strains, which constitutively synthesize C- ribosomes
161 (Fig. S2). To determine the effect of zinc-responsive ribosome hibernation on Rsh-
162 ribosome interaction, we analyzed the impact of Mpy recruitment factor (Mrf) on Rsh
163 stability, activity, and its occupancy on the ribosome. Mrf inhibits translation and growth
164 of cells, likely by sequestering SSU to promote Mpy recruitment (Li *et al.*, 2020).
165 Deletion of *mrf* in zinc-starved *M. smegmatis* restored the levels of intracellular and
166 ribosome bound Rsh to those in high-zinc wildtype cells, and the mutant phenotype was
167 complemented by plasmid-borne *mrf* (Fig. 2A-B). Increase in Rsh abundance in zinc-
168 starved Δ*mrf* also corresponded to an increase in ppGpp levels upon exposure to TBST
169 (Fig. 2C). Together, these data are consistent with figure 1C towards the conclusion that
170 the limiting intracellular free zinc concentration has little direct impact on the stringent
171 response, while accumulation of Mrf induced by zinc depletion and likely sequestration
172 of ribosomes for hibernation inhibits Rsh-ribosome interaction and decreases total Rsh
173 abundance in the cell. Interestingly, deletion of Rsh did not impact Mpy-ribosome
174 interaction (Fig. S3), distinguishing mycobacteria from other species in which ppGpp
175 transcriptionally induces factors necessary for ribosome hibernation (Hood et al., 2016;
176 Izutsu et al., 2001; Schafer et al., 2020).
177

178 *Ectopic expression of Mrf can reduce intracellular abundance of Rsh.*

179 To further validate Rsh instability, and thus its activity, by Mrf in *M. smegmatis*, we
180 asked how an ectopic expression of Mrf would impact Rsh levels in the cell. We
181 exploited a stable Mrf variant (Mrf*), which has reduced zinc affinity, and is recalcitrant
182 to regulation by the Clp protease system (Li *et al.*, 2020). Consequently, constitutive
183 transcription of Mrf* leads to its substantial accumulation in high-zinc mycobacteria,
184 presumably in a conformation that is capable of binding to the ribosome and inhibiting
185 growth (Li *et al.*, 2020). The effect of ectopic accumulation of Mrf* on Rsh association
186 with the ribosome was determined using an acetamide-based heterologous expression
187 system in high-zinc cultures of *M. smegmatis*. Figure 2D shows that expression of Mrf*
188 in high-zinc cells led to concomitant loss of Rsh, both in the lysates (Fig. 2D) and on the
189 ribosome (Fig. 2E).

190 Because SpoT in *Salmonella enterica* was identified as a potential substrate of
191 the Clp protease system (Gao et al., 2019), we tested the possibility whether
192 mycobacterial ClpP1P2 protease could be involved in regulating the abundance of free
193 Rsh in cells. The *M. smegmatis* strain YL9 (Li *et al.*, 2020) harboring CRISPRi-based
194 system for conditional depletion of ClpP1, while constitutively transcribing FLAG-tagged
195 Mrf, was used to test whether Rsh loss during Mrf stabilization is Clp-dependent.
196 Depletion of ClpP1 in high-zinc cells resulted in concomitant accumulation of both Mrf
197 and Rsh (Fig. 2F). Thus, loss of Rsh in cells during Mrf stabilization is likely achieved
198 through a Clp-dependent mechanism, although whether Rsh is a direct substrate of Clp
199 remains to be determined.

200 *Interaction with the ribosome is necessary for intracellular stability of Rsh*

201 The loss of intracellular Rsh abundance in cells with hibernating ribosomes reveals its
202 instability, while raising the question as to how it is stabilized . Interestingly, we
203 observed similar levels of Rsh-bound ribosomes in high-zinc cultures before and after
204 the TBST exposure (Fig. S4), which suggest an interaction between Rsh and ribosome
205 even during a basal level of ppGpp synthesis. We therefore tested whether interaction
206 with the ribosome impacts the intracellular stability of Rsh. *E. coli* RelA interacts with the
207 ribosome primarily through its CTD containing a conserved CCHC type zinc-finger in the
208 ZBD, which makes extensive contacts with the inter-subunit region of the 70S ribosome,
209 and ASF of LSU (Brown *et al.*, 2016; Kudrin et al., 2018). Although the requirement of
210 zinc in RelA-ribosome interaction remains unclear, the zinc coordinating residues
211 $C_{612}C_{613}H_{634}C_{638}$ ($C_{666}C_{667}H_{688}C_{692}$ in *M. smegmatis Rsh*) of ZBD are conserved in
212 mycobacteria and likely acquire the same three-dimensional conformation as in *E. coli*
213 RelA (Fig. 3A). Furthermore, Rsh_{C633A} variant in *M. tuberculosis* (C692 in *M. smegmatis*)
214 is catalytically impaired *in vitro* (Avarbock *et al.*, 2005), supporting its important role in
215 Rsh activity. We therefore mutated the key ZBD residues and studied the impact on the
216 intracellular abundance of Rsh. Substitution of C_{666} and C_{692} residues resulted in
217 substantial loss of Rsh in both the cell lysate and on the ribosome in actively growing *M.*
218 *smegmatis* cells in zinc-rich condition (Fig. 3B). Presence of wildtype Rsh on the
219 ribosome was unambiguous (Fig. 3B), supporting an argument that Rsh-ribosome
220 interaction in non-starved cells is constitutive. Substitution in the adjacent D_{691} neither
221 impacted the Rsh-ribosome interaction nor the intracellular abundance of the protein

222 (Fig. 3B). Recombinant expression of these Rsh variants in *E. coli* did not significantly
223 impact the protein yield (Fig. S5), implying that these mutations do not affect the
224 inherent stability of the protein *in vivo*, and their properties are likely determined by the
225 intracellular environment of mycobacteria. To further test if the mutations specifically
226 disrupted Rsh-ribosome interaction in mycobacteria, we mixed recombinant Rsh_{C666G}
227 and Rsh_{C692F} variants with 70S ribosomes purified from Δ*rsh* mutant of *M. smegmatis*
228 and analyzed their occupancy on the ribosome separated from the free protein by
229 ultracentrifugation on a 32% sucrose cushion. Compared to the wild-type Rsh,
230 association with the ribosome was significantly compromised for both recombinant
231 proteins, $rRsh_{C666G}$ and $rRsh_{C692F}$ (Fig. 3C). We thus conclude that Rsh constitutively
232 interacts with the ribosome using its ZBD in non-starved cells, and this interaction is
233 necessary for the intracellular stability of the enzyme.
234
235 *Rsh interacts with the IF2 bound 70S initiation complex*
236 We next focused on understanding the stage of translation when Rsh would most likely
237 interact with the ribosome in a non-starved cell. We streamlined our approach based on
238 the published structures (Arenz *et al.*, 2016; Brown *et al.*, 2016; Loveland *et al.*, 2016),
239 which delineate permissive and non-permissive translation complexes for RelA binding.
240 While RelA can bind to a late translation initiation intermediate (70S- fMet-$tRNA_i^{Met}$ -
241 mRNA with vacant A-site) (Loveland *et al.*, 2016), its binding to the ribosome during
242 translation elongation is expected to be sterically hindered by inter-subunit rotation
243 (Arenz *et al.*, 2016; Brown *et al.*, 2016; Loveland *et al.*, 2016). We therefore

244 hypothesized that mycobacterial Rsh would enter the translation initiation complex
245 through one of the free ribosomal subunits and likely remain on the complex until the
246 start of the first cycle of elongation. This hypothesis also implies that Rsh must remain
247 associated with the ribosome during its transition from initiation to pre-elongation
248 stages, without affecting the canonical conformation of the translation complex.
249 To investigate this possibility, we first determined the propensity of Rsh to
250 interact with free ribosomal subunits. When purified recombinant Rsh was mixed
251 individually with each of the two purified factor-free ribosomal subunits and the
252 macromolecules were separated on 32% sucrose cushion, Rsh appeared to
253 preferentially co-sediment with LSU (Fig. 4A). We next asked if Rsh would remain in the
254 translation complex during its transitions through various intermediate stages of
255 initiation, especially given the potential of a steric clash between Rsh and translation
256 initiation factor 2 (IF2). The contact points of IF2 on the 70S initiation complex
257 significantly overlaps with those of Rsh (Arenz *et al.*, 2016; Brown *et al.*, 2016; Loveland
258 *et al.*, 2016; Sprink et al., 2016). We therefore tested the ability of Rsh to interact with
259 the ribosome in the presence of IF2, fMet-tRNA$_i^{Met}$ and mRNA *in vitro*. Dissociated
260 ribosomes (Fig. S6) were mixed with His$_6$-IF2, His$_6$-Rsh, fMet-tRNA$_i^{Met}$, leadered mRNA,
261 and either GTP or a non-hydrolysable analogue (GMP-PNP). The assembled 70S
262 complex purified on 10-40% sucrose density gradient (SDG) was analyzed for the
263 presence of IF2 and Rsh. The 70S ribosomes assembled in the presence of GTP
264 contained Rsh, but undetectable levels of IF2 (Fig. 4B), demonstrating that Rsh can
265 associate with the ribosome in the presence of the canonical ligands without interfering

266 with GTP-dependent release of IF2 (Marshall et al., 2009). This property of
267 mycobacterial Rsh was in sharp contrast to *B. subtilis* Rsh, which cannot form a stable
268 complex with the ribosome without an A-site deacyl-tRNA (Takada *et al.*, 2021).
269 Unexpectedly, both Rsh and IF2 were detected in 70S particles assembled in the
270 presence of GMP-PNP (Fig. 4C), suggesting that perhaps one or both the proteins
271 could be occupying the ribosome in their non-canonical conformations.
272
273 *Cryo-EM structure reveals a hitherto unknown ribosome-Rsh interactions*
274 To gain further insight into the Rsh-bound *M. smegmatis* 70S ribosome in a translation
275 initiation complex, we performed single-particle cryo-EM to determine the structure of
276 the 70S ribosome assembled in the presence of IF2, Rsh, fMet-tRNA$_i^{Met}$, leadered
277 mRNA, and GMP-PNP. 3D classification of the cryo-EM dataset (Figs. S7, S8, Table
278 S3) revealed a unique Rsh-bound state in which the ribosome is in a classical non-
279 rotated state, but none of the classes showed any density for IF2. The Rsh-bound 3D
280 class refined to 2.7 Å resolution showed densities only for two C-terminal domains of
281 Rsh, ZBD and ACT, along with a fMet-tRNA$_i^{fMet}$ bound at the ribosomal P site, while
282 remainder of the Rsh domains were found to be disordered (Figs. 4D, 4E, S7 and S9).
283 The ZBD interacts with the components of both SSU and LSU: SSU protein uS19 and
284 the LSU 23S rRNA helix H38 (also referred to as ASF) (Fig. 4E). These interactions
285 resemble those reported in the structures of *E. coli* RelA and *B. subtilis* Rsh on the
286 ribosome (Loveland *et al.*, 2016; Pausch et al., 2020). The Rsh-ACT domain occupies

287 the inter-subunit space and interacts with LSU proteins uL16, uL11, and the 23S rRNA
288 helices H43-44 at the base of the protein L7/L12 stalk (Fig. 4E).
289 To understand a possible spatial interaction between IF2 and Rsh in *M.*
290 *smegmatis* 70S ribosome, we superimposed either our structure or *E. coli* 70S
291 ribosome-RelA (Loveland *et al.*, 2016) with 70S-IF2-GMP-PNP initiation complexes
292 (Sprink *et al.*, 2016). Indeed, RelA's alpha-helical domain (AHD) which is followed by
293 the ZBD, and the ACT domain in its canonical conformation bound to A/R tRNA
294 (Loveland *et al.*, 2016) would directly clash with domain VI-C1 of IF2 (Fig. 4F). In tertiary
295 structure, the AHD lies adjacent to the ACT domain while the ZBD is anchored to the
296 ribosome via its interactions with uS19 and ASF. Moreover, in our structure the ACT
297 domain was rotated with respect to ZBD by ~14 degrees, presumably to prevent the
298 clash between AHD and domain VI-C1 of IF2 (Fig. 4F). Across the reported structures
299 (Loveland *et al.*, 2016; Pausch *et al.*, 2020) the ACT domain is known to exhibit some
300 conformational variations as compared to the ZBD domain, although a rotation by 14
301 degrees is unprecedented. It is possible that the adopted conformation of the ACT
302 domain in our structure is to accommodate the exiting IF2 molecule immediately upon
303 completion of the translation initiation phase.
304 Compared to the *E. coli* RelA and *B. subtilis* Rsh, mycobacterial Rsh shows an
305 overall similarity in tertiary structures of ZBD and ACT domains, although the rotation of
306 the ACT domain translates into its shift by ~6 Å towards the LSU's L7/L12 stalk base
307 (Fig. 5A, B). This altered conformation of ACT is stabilized through extensive
308 interactions with the uL11 and the 23S rRNA helices H43/44 (Fig. 5C). Specifically,

309 uL11 lysines, 89 and 96 interact with Y791, D789 and H776 of Rsh-ACT. Further, Rsh-
310 ACT S779, N783, D789 and Y788 interact with the 23S rRNA helices H43-44
311 phosphate backbones. These interactions are in sharp contrast to the *E. coli* ribosome-
312 RelA structures, where uL11 interacts with the A/R tRNA but not directly with RelA
313 (Loveland *et al.*, 2016). Thus, our structure reveals a unique conformational state of the
314 ribosome-bound Rsh. Multiple sequence alignment of the amino acid sequences does
315 not reveal any apparent substitutions, insertions, or deletions that can explain the
316 altered orientation of the ACT domain in *M. smegmatis* Rsh (Fig. S10). Given that our
317 structure was obtained in the presence of IF2-GMP-PNP, a key difference from the *E.*
318 *coli* ribosome-RelA complex, a possible role of IF2 in inducing the rotation of ACT
319 cannot be ruled out.

320 The superimposition also reveals some species-specific differences, which could
321 manifest as differences in Rsh/RelA-ribosome binding affinities (Fig. S10). The ZBD
322 domains interact with uS19 and ASF in all three cases, however, compared to *M.*
323 *smegmatis*, *B. subtilis* Rsh has additional interactions — two with uS19, one with ASF,
324 and one with uS13 (Fig. S10). Loss of the additional interactions with uS19 and ASF in
325 *M. smegmatis* is likely due to substitution at corresponding positions with non-polar
326 amino acids (Fig. S10). However, *M. smegmatis* Rsh-ZBD could potentially interact with
327 uS13 since it has an Arg (R681) corresponding to K617 in *B. subtilis*. The *E. coli* RelA
328 ZBD also has two additional interactions compared to *M. smegmatis*, one with uS19 and
329 the other with ASF (Fig. S10). However, *E. coli* RelA ZBD has a Gln (Q627)
330 corresponding to R681 and K617 in *B. subtilis* and *M. smegmatis*, respectively, which

331 might not interact with uS13 due to its shorter side chain. Since the density
332 corresponding to ZBD is relatively strong in our structure, we designate it as the primary
333 anchoring domain of mycobacterial Rsh.
334 Interactions stabilizing Rsh in our structure are primarily through LSU's ASF,
335 uL16, uL11, and rRNA helices H43/44, suggesting that Rsh associates primarily with
336 the LSU, corroborating the results of our binding experiments that shows association of
337 Rsh with free LSU. Moreover, uL11 and rRNA helices H43/44 together constitute the
338 L7/L12-stalk base of LSU and are known to be mobile during elongation (Datta et al.,
339 2005) and recycling (Yokoyama et al., 2012) phases of translation. We thus surmise
340 that intensive contacts between L7/L12-stalk base and the Rsh-ACT domain would
341 transiently lock the ribosome in a stalled state before the start of translation elongation
342 cycle, as a mechanism to survey the aminoacylation state of the incoming tRNA to the A
343 site. A direct contact of Rsh with uL11 is distinct from *E. coli* RelA, binding of which is
344 independent of uL11 while (p)ppGpp synthesis requires uL11 and a deacylated-tRNA at
345 the A-site (Friesen et al., 1974; Parker et al., 1976; Wendrich *et al.*, 2002; Yang and
346 Ishiguro, 2001). While the changes in *M. smegmatis* complex here could be induced by
347 the presence of IF2, we cannot exclude the possibility that these interactions or the ACT
348 conformation are specific *to M. smegmatis* Rsh.
349
350 *Can Rsh bind to a hibernating ribosome?*
351 Given that interaction with the ribosome is necessary for the intracellular stability of Rsh,
352 its loss in cells harboring Mrf, and therefore Mpy-bound hibernating ribosomes, suggest

353 that these ribosomes are perhaps inaccessible to free Rsh. To further probe this
354 possibility, superimposed the structures of Mpy-bound and Rsh-bound 70S ribosomes.
355 Mpy and Rsh bind at two physically distinct sites on the unrotated SSU of the ribosome
356 (Fig. 6A). Mpy N-terminal domain binds to SSU spanning the decoding center by
357 interacting extensively with the 16S rRNA components that converge from platform,
358 body, and head regions at the SSU's neck (Li *et al.*, 2018). Rsh ZBD on the other hand
359 interacts near the inter-subunit bridge B1a (Gabashvili et al., 2000) forming
360 components, including uS19 of SSU and LSU's ASF (Gao *et al.*, 2019) (Figs. 4E and
361 6A). Since the binding sites of the two factors do not overlap, we superimposed the
362 structures of Rsh- and Mpy-bound *M. smegmatis* 70S ribosomes to understand the
363 accessibility of Mpy-bound hibernating ribosome to Rsh binding. Despite both the
364 ribosomes being in their unrotated state, the SSU head domain in the Rsh-bound
365 structure is tilted more towards the LSU in comparison to the Mpy-bound ribosome
366 structure (Fig. 6B). The untilted SSU head in the MPY-bound state will prevent
367 interactions of Rsh-ZBD with uS19 (Fig. 6C). Since ZBD is the primary anchoring
368 domain of Rsh (Loveland *et al.*, 2016; Pausch *et al.*, 2020), any alteration in bridge B1a
369 configuration in the Mpy-bound state is likely to directly inhibit Rsh binding, thereby
370 exposing Rsh to proteolytic degradation. Thus, loss in the overall pool of intracellular
371 Rsh during ribosome hibernation could be a combined outcome of both a decrease in
372 the synthesis of new Rsh and the occlusion of pre-existing Rsh from the hibernating
373 ribosome.
374

375 **Discussion:**

376 The stringent response, characterized by Rsh-dependent synthesis of (p)ppGpp and
377 subsequent transcriptional reprogramming by the alarmone, is among the central
378 adaptation mechanisms in nutrient-starved mycobacteria. Yet, a significant knowledge
379 gap exists in the mechanism underlying starvation sensing by Rsh. Structural studies
380 with *E. coli* RelA offer mechanistic details about Rsh activation by the presence of
381 deacylated-tRNA at the A- site in a stalled translation elongation complex, although it
382 remains unclear how Rsh would encounter such a complex *in vivo*. Two models have
383 emerged from recent studies: a) the hopping model in which Rel-deacylated-tRNA
384 complex is formed prior to its entry at the A- site of the elongation complex (Winther *et*
385 *al.*, 2018), and b) starvation-induced formation of a weak RelA-ribosome complex prior
386 to its stabilization by deacylated-RNA (Takada *et al.*, 2021). Both models however
387 preclude RelA-ribosome interaction in non-starved cells, which is inconsistent with the
388 evidence of constitutive RelA-ribosome interaction throughout the growth of *E. coli* and
389 *P. aeruginosa* cells (English *et al.*, 2011; Pletzer et al., 2020). These discrepancies
390 suggest more complex scenarios that need further clarification. Here, we propose a new
391 model of Rsh recognition of a paused translation elongation complex in mycobacteria.
392 In this model, which we call the surveillance model, Rsh constitutively interacts with
393 translating ribosomes during the formation of the initiation complex, and its transition to
394 the pre-elongation stage (Fig. 7). Presence of Rsh in a pre-elongation translation
395 intermediate would arguably trigger (p)ppGpp synthesis upon entry of a deacylated-
396 tRNA at the A- site during the first cycle of elongation, while entry of a cognate amino

397 acylated-tRNA and normal cycle of elongation accompanied by inter-subunit rotation
398 would likely displace Rsh from the complex (Arenz *et al.*, 2016; Brown *et al.*, 2016;
399 Loveland *et al.*, 2016). Free Rsh appears to be labile and must associate with
400 ribosomes entering the translation cycle, or a paused elongation complex with
401 deacylated-tRNA at the A- site (Fig. 7), although the latter interaction would arguably be
402 less frequent. A rapid rate of translation in an actively growing cell would likely maintain
403 a sufficiently large pool of free ribosomes, transitioning between termination and
404 initiation cycles, to ensure a stable population of Rsh-ribosome complex. The
405 surveillance model of the stringent response activation is arguably less stochastic than
406 the hopping model.
407 Lack of Rsh under conditions such as those inducing ribosome hibernation
408 further supports the model that optimum protein synthesis and accessibility to
409 translating ribosomes is critical for the intracellular stability of Rsh. This finding further
410 differentiates the physiological conditions for ribosome hibernation and the stringent
411 response. The negative impact of Mpy-dependent ribosome hibernation on the stringent
412 response also highlights a unique relationship between the two central adaptation
413 mechanisms in mycobacteria in a zinc-responsive manner. This relationship further
414 implies that the stringent response is an upstream adaptation response relative to
415 ribosome hibernation; arguably a logical order given that the stringent response
416 reprograms the gene expression to fine-tune the metabolism, while ribosome
417 hibernation directly shuts down global protein synthesis altogether. Moreover,
418 restoration of (p)ppGpp synthesis in zinc-depleted Δ*mrf* or Δ*mpy* implies that Rsh-

419 ribosome interaction and Rsh activation are relatively more resilient to intracellular
420 depletion of free zinc, despite that the zinc coordinating residues are crucial for Rsh
421 function. Perhaps the affinity for zinc in Rsh is too strong to be affected by global
422 depletion of free zinc and may even support activation of the stringent response under
423 moderately low-zinc condition that is not severe enough to induce Mpy-dependent
424 ribosome hibernation. Zinc is an essential nutrient that binds to 6-10% of all proteomes
425 in bacteria (Andreini et al., 2006), likely impacting the function of multiple proteins
426 including RNA polymerase β' subunit (Hu and Liu, 2022), and several amino acyl tRNA
427 synthetases (aaRS) (Andreini *et al.*, 2006). Lack of zinc in the active site of ThrRS
428 inactivates the aminoacylation activity of the enzyme (Sankaranarayanan et al., 1999).
429 Thus, intracellular availability of zinc in mycobacteria could be a shared signal for
430 sequential onset of the two adaptive responses mediated directly through sensing the
431 translation activity of the ribosome. The sequential relationship between the stringent
432 response and ribosome hibernation could possibly occur even in other nutrient-starved
433 conditions that induce both the adaptation pathways.
434 The Clp-dependent loss of ribosome-free intracellular Rsh, while reaffirming the
435 tight regulation of ppGpp synthesis in cells, does not entirely rule out the CTD-
436 dependent autoinhibition of the synthase activity through oligomerization: a model
437 primarily proposed from *in vitro* characterization of the enzyme (Avarbock *et al.*, 2005;
438 Gropp *et al.*, 2001; Jain *et al.*, 2006). However, the evidence of ribosome-bound Rsh as
439 the dominant species suggests that Rsh oligomers, if any, would be a minor molecular
440 species *in vivo*. Moreover, the requirement of CTD in oligomerization *in vitro* (Avarbock

441 *et al.*, 2005) suggest that formation of the oligomeric form is perhaps outcompeted *in*
442 *vivo* by a stronger affinity of the CTD for the ribosome than for another Rsh CTD. The
443 likely predominance of ribosome-bound Rsh *in vivo* further raises the possibility that a
444 reversible transition between synthase and hydrolase activities may occur without the
445 CTD-dependent autoinhibition mechanism, perhaps through differential allosteric effects
446 of ppGpp and GDP/ATP binding to the hydrolase and the synthase domain,
447 respectively, as shown by Tamman et al. (Tamman *et al.*, 2020). The CTD however
448 could modulate the enzymatic activity of Rsh through its interaction with the ribosome,
449 perhaps like the *B. subtilis* Rsh (Takada *et al.*, 2020). In summary, this study highlights
450 that the *in vitro* biochemical studies may have limitations in understanding the function
451 and regulation of mycobacterial Rsh, while offering new framework for further
452 investigation of the interrelationship between the stringent response and ribosome
453 hibernation in mycobacteria.
454

455 **Experimental Procedures:**

456 **Bacterial growth medium**

457 *Mycobacterium smegmatis* (mc^{2}155) and its variant strains were grown on a shaker at
458 200 rpm at 37 °C in Middlebrook 7H9 + 10%ADC + 0.05% Tween80 until required. For
459 experiments related to ribosome purification, cells from saturated culture were washed
460 with PBS + 0.05% Tween80 for three times and then inoculated at 1:100 dilution in
461 Sauton's medium with either 1 mM $ZnSO_4$ or 1 µM zinc-chelator (TPEN, N,N,N',N'-
462 Tetrakis(2-pyridylmethyl)ethylenediamine) as specified. 7H10ADC agar plate was used
463 for selection of recombinants and colony growth (*M. smegmatis*). Pellicle biofilms of
464 *Mycobacterium tuberculosis* (mc^{2}7000) were cultured in detergent-free Sauton's medium
465 either with 1mM $ZnSO_4$ or without supplemental zinc. Cells from a 40 µL aliquot of a
466 saturated planktonic culture in 7H9 medium with 10% OADC and 0.05% Tween-80 were
467 inoculated into 4 mL of detergent-free Sauton's medium in a 12-well polystyrene plate
468 and incubated without shaking for 7-weeks at 37 °C. 100 µg/mL pantothenate was added
469 for cultures of *Mycobacterium tuberculosis* (mc^{2}7000). *Escherichia coli* (GC5 or BL21)
470 was grown in LB broth or LB agar at 37 °C. Zeocin (25 µg/mL), kanamycin (20 µg/mL),
471 hygromycin (150 µg/mL for *M. smegmatis* and *E. coli*, or 50 µg/mL for *M. tuberculosis*),
472 carbenicillin (50 µg/mL), and apramycin (5 µg/mL) were used for selection as necessary.
473

474 **Construction of recombinant plasmids and strains**

475 List of plasmids, bacterial strains in this study are provided in Table S1. List of
476 oligonucleotides are provided in Table S2. For construction of Δ*rsh* in *M. smegmatis*, the

477 gene was replaced with a zeocin-resistance marker using a PCR-based modified version
478 of the recombineering strategy as previously described (Li *et al.*, 2018). For analyzing
479 the stability of wildtype or $C_{666}G$, $D_{691}R$ and $C_{692}F$ variants of Rsh, wildtype Rsh ORF with
480 500 bp ustream sequence was PCR-amplified and cloned into KpnI-XbaI sites of an
481 integrative vector pMH94, resulting in a recombinant plasmids pYL238. Mutations at
482 respective sites were introduced using pYL238 as template by PCR-based mutagenesis
483 using primers listed in Table S2, resulting in pYL240 ($C_{666}G$), pYL241 ($D_{691}R$) and pYL242
484 ($C_{692}F$). The plasmids pYL238, pYL240, pYL241 and pYL242 were electroporated into
485 Δ*rsh* strain of *M. smegmatis*. The recombinant strains were cultured in nutrient-rich
486 medium and analyzed for Rsh levels by immunoblotting as described.
487

488 **Recombinant protein expression and purification**

489 Rsh from *M. smegmatis* (Msmeg_2965) and its variants (Rsh_{C666G}, Rsh_{D691R} and
490 Rsh_{C692F}) with N-terminal His tag fusion were cloned in pET21b vector using NdeI and
491 HindIII. The recombinant plasmids were introduced into BL21 (DE3) pLysS cells for
492 recombinant Rsh expression and purification. Briefly, the cells were grown in LB medium
493 to log phase (OD_{600} around 0.7) at 37 °C when RSH expression was induced with 0.5 mM
494 IPTG for 4 hours at 37 °C. Induced cells were harvested (8000 rpm, 20 minutes, RT in
495 Thermo Scientific™ Fiberlite™ F12-6 × 500 Fixed-Angle Rotor) and then resuspended in
496 N-I buffer (50 mM Tris (pH 8.0), 300mM NaCl, 5% glycerol, 10 mM imidazole, 1mM
497 PMSF). The cells were further sonicated (Amplitude 30%, 10 sec on/off for 60 minutes)
498 at 4 °C and the soluble protein in the supernatant was separated from the debris by

499 centrifugation (13000 rpm 20 minutes, 4 °C in Thermo Scientific™ Fiberlite™ F12-6 × 500
500 Fixed-Angle Rotor) and incubated with pre-equilibrated Ni-NTA resin for 1 hour at 4 °C.
501 After incubation, Ni-NTA resin was washed three times with N-II buffer [50 mM Tris (pH
502 8.0), 300mM NaCl, 5% (v/v) glycerol, 30 mM imidazole]. Rsh was then eluted with
503 stepwise increments of imidazole (from 60 mM to 100mM and to 250 mM) in a buffer
504 containing 50 mM Tris (pH 8.0), 300mM NaCl and 5% (v/v) glycerol. Fractions with the
505 purest proteins were pooled and imidazole was removed by dialysis in the buffer
506 containing 50 mM Tris (pH 8.0), 300mM NaCl and 30% (v/v) glycerol. For recombinant
507 IF2 with N-terminal His_{6x} tag, the full-length codon optimized gene with N-terminal 6X-
508 His-sequnce and NdeI-XhoI sites was synthesized (IDTDNA Inc.) (see the sequence after
509 Table S2), and clone into a pET21a vector. Recombinant protein was expressed in BL21-
510 DE3 pLysS) and purified on Ni-NTA matrix as detailed for His_6-Rsh above.
511
512 **Ribosome purification**
513 Rsh bound ribosomes were purified with few modifications from the previously described
514 protocol (Li *et al.*, 2018). *M. smegmatis* cells were grown for specified time in 500 mL of
515 Sauton's media containing 0.05% Tween 80 and either 1 mM $ZnSO_4$ or 1 μM TPEN. Cells
516 were harvested (8000 rpm for 20 minutes in Thermo Scientific™ Fiberlite™ F12-6 × 500
517 Fixed-Angle Rotor) and pulverized 6 times at 15 Hz for 3 minutes in a mixer mill (Retsch
518 MM400). The lysates were mixed with 20 mL of HMA-10 buffer (20 mM HEPES-K pH7.5,
519 30 mM NH_4Cl, 10 mM $MgCl_2$, 5 mM β-mercaptoethanol) and centrifuged for 30 minutes
520 at 30,000 g in Thermo Scientific™ Fiberlite™ F12-8 × 50 Fixed-Angle Rotor. The

521 supernatants were collected in the Beckman PC ultracentrifuge tubes and further
522 centrifuged for 2 hours and 15 minutes at 42800 rpm in a Beckman rotor Type 70Ti.
523 Pellets were soaked in 4 mL of HMA-10 buffer in an ice water bath overnight, and then
524 homogenized for 30 minutes. Then the homogenized pellets were treated with 3 units/mL
525 Rnase-free Dnase (Ambion) for two hours at 4 °C. The contents were transferred to
526 Beckman PA tubes centrifuged at 22,000 g for 15 minutes in Thermo Scientific™
527 Fiberlite™ F12-8 × 50 Fixed-Angle Rotor. Supernatants were collected into Beckman
528 ultracentrifuge PC tubes and centrifuged for 2 hours and 15 minutes at 42,800 rpm in a
529 Beckman rotor Type 70Ti. Pellets were dissolved in 1 mL HMA-10 buffer and centrifuged
530 for 10 minutes at 10,000 g. Supernatants containing the crude ribosomes were collected
531 and quantified by measuring their optical density at 260 nm. The crude ribosome
532 preparations were then layered on top of 37 mL sucrose density gradients (10%-40%)
533 and centrifuged for 16 hours at 24,000 rpm in a Beckman rotor SW 28. The 70S ribosome
534 fractions were collected after fractionating the sucrose gradient in a 260 nm Brandel
535 gradient analyzer as previously described (Li et al., 2021a). The pooled 70S ribosome
536 fractions pelleted by ultracentrifugation at 42,800 rpm for 3 hours in a Beckman rotor Type
537 70Ti were suspended in HMA-10 buffer (20 mM HEPES-K pH7.5, 30 mM NH_4Cl, 10 mM
538 $MgCl_2$, 5 mM β-mercaptoethanol) and quantified by measuring absorbance at 260 nm.

539 MPY-bound ribosomes and other high-salt washed ribosomes were purified
540 exactly as described previously (Li *et al.*, 2020; Li *et al.*, 2018). The steps up to
541 homogenization were same as described above. After homogenization, 4 mL of the
542 homogenized suspension was treated with 3 units/mL Rnase-free Dnase (Ambion) for

543 one hour at 4 °C, then 4 mL of HMA-0.06 buffer (20 mM HEPES-K pH 7.5, 600 mM NH_4Cl,
544 10 mM $MgCl_2$, 5 mM β-mercaptoethanol) was added to the suspension, which was further
545 incubated at 4 °C for 2 hours. The content was transferred to Beckman PA tubes and
546 centrifuged at 22,000 g for 15 minutes in Thermo Scientific™ Fiberlite™ F12-8 × 50 Fixed-
547 Angle Rotor. Supernatants were collected and layered on top of 8 mL 32% sucrose
548 solution in HMA-10 buffer and centrifuged for 16 hours at 37000 rpm in a Beckman rotor
549 Type 70Ti. The supernatant was discarded, and the pellet was rinsed with HMA-10 buffer
550 to remove the brownish material. The crude ribosome was resuspended in 1 mL HMA-10
551 buffer and centrifuged for 10 minutes at 10,000 g. Supernatant containing the crude
552 ribosome was collected and quantified by measuring optical density at 260nm. 70S
553 ribosome from crude ribosome was further separated on a 10-40% sucrose density
554 gradient and fractionated as indicated above.

555

556 **In vitro reconstitution of Rsh with 70S initiation complex**

557 *Co-sedimentation of Rsh with the ribosomal subunits:* 70S ribosomes were purified from
558 low-zinc culture of isogenic Δ*rsh*/Δ*mpy*/Δ*mrf* triple mutant of *M. smegmatis*. Subunits were
559 dissociated from the purified 70S ribosomes by incubation at 37°C for thirty minutes in
560 HMA-1 buffer (20 mM HEPES-K pH7.5, 30 mM NH_4Cl, 1 mM $MgCl_2$, 5 mM β-
561 mercaptoethanol. The resulting subunits were then purified from a 10-40% sucrose
562 density gradient. Individual subunits equivalent to A_{260} of 0.3 (7.2 pmol) were mixed with
563 1.8 pmol of purified recombinant Rsh in 100 μL binding buffer (20 mM HEPES-K pH7.5,
564 100 mM NH4Cl, 10 mM $MgCl_2$, 5 mM β-mercaptoethanol, 50mM KCl), and the mixture

565 was incubated for thirty minutes at 37°C. The reactions were then layered on 100 μL of
566 32% sucrose cushion and centrifuged at 42,800 rpm for 3 hours in a Beckman TLA 100
567 rotor using the Optima-Max TL ultracentrifuge (Beckman Coulter). After centrifugation,
568 the supernatant was discarded, and the ribosome pellet was resuspended in 20 μL HMA-
569 10 buffer. The abundance of Rsh was further determined by immunoblotting using the
570 protocol described below Rsh, and S13, and L33.
571 *Preparation of fMet-tRNA$_i^{Met}$:* An *E. coli* culture containing a plasmid borne expression
572 vector for tRNA$_i^{Met}$ under control of the LacI repressor was grown to an optical density at
573 600 nm of 0.4-0.6 at which time IPTG was added to induce expression of the tRNA.
574 After 8 h the cells were harvested, lysed by phenol, and total tRNA isolated using a
575 series of differential precipitation steps (Ehrenstein, 1967). Approximately half of the
576 recovered tRNA was a substrate for charging by MetRS. The charging reaction (2 mL)
577 contained approximately 200 nmoles of total tRNA and 10 nmoles of MetRS in the
578 presence of 1 mM methionine, 2 mM ATP, 10 mM $MgCl_2$, 20 mM KCl, 4 mM DTT, 50
579 μg/mL BSA, and 50 mM Tris-HCl pH 7.5. After 10 min at 37 °C a 4.0 μL aliquot of the
580 reaction was removed for determination of the charging efficiency as described by
581 Gamper et *al* (Gamper and Hou, 2020). The remaining reaction was incubated for 10
582 min at 37 °C with 1.7 *μ*moles of 10-formyltetrahydrofolate and 20 nmoles of methionyl
583 formyl transferase to convert Met-tRNA$_i^{Met}$ to fMet-tRNA$_i^{Met}$. The reaction was quenched
584 by adding a 0.1 volume of 2.5 M NaOAc pH 5.0. Following an equal volume pH 5
585 phenol-chloroform-isoamyl alcohol extraction (80:17:3), the tRNA was ethanol

586 precipitated, dissolved in 300 μL 25 mM NaOAc pH 5.0, and stored at -70 ^{o}C.
587 Approximately 200 nmoles of tRNA was recovered, of which 45% was fMet-$tRNA_i^{Met}$.
588 *Reconstitution of Rsh-bound 70S initiation complex: 70S* ribosomes prepared from a
589 low-zinc culture of isogenic Δ*rsh*/Δ*mpy*/Δ*mrf* triple mutant of *M. smegmatis* were
590 dialyzed at 4°C with low-magnesium buffer (20 mM HEPES-K pH7.5, 30 mM NH_4Cl, 0.5
591 mM $MgCl_2$, 5 mM β-mercaptoethanol) to dissociate the 30S and 50S subunits. Two
592 rounds of dialysis were performed, with fresh buffer change every four hours. Subunit
593 dissociation was confirmed by loading 2.4 picomoles of the dialyzed ribosomes onto a
594 10-40% sucrose density gradient. Another 2.4 pmoles of dissociated ribosomes were
595 mixed with five-fold molar excess of fMet-$tRNA_i^{fMet}$, a synthetic mRNA template
596 (GGCAAGGAGGUAAAAAUGUUCAAAAAA-Flour) (IDT, USA), recombinant His_6-IF2,
597 recombinant His_6-Rsh, and either GTP or GMP-PNP (Sigma-Aldrich) in a 100 µL
598 reaction in buffer I (20 mM HEPES-K pH 7.5, 30 mM NH_4Cl, 1 mM $MgCl_2$, 5 mM β-
599 mercaptoethanol), and the mixture was incubated at 37 °C for 15 minutes to allow
600 formation of the initiation complex on the 30S subunit. Then 25 µL of buffer II (20 mM
601 HEPES-K pH7.5, 30 mM NH4Cl, 50 mM MgCl2, 5 mM β-mercaptoethanol, 600mM KCl)
602 was added to the mixture, thereby bringing the final concentration of $MgCl_2$ and KCl to
603 10mM and 120 mM, respectively. The reaction was then incubated for an additional 30
604 minutes at 37°C to allow joining of the 50S subunit. Resulting complexes were either
605 used for structural analysis or resolved on a 15 mL 10-40% sucrose density gradient
606 centrifuged at 35000 rpm for 135 minutes using SW41 rotor on an Optima L-90K
607 ultracentrifuge (Beckman Coulter), and the resolved particles were fractionated as

608 previously described (Li *et al.*, 2021a). For immunoblotting analysis, content of the
609 indicated fractions were precipitated using Methanol-chloroform extraction as previously
610 described (Li *et al.*, 2020). Briefly, each fraction was vortexed with 4X volume of
611 methanol for 5-10 seconds and centrifuged for 10 seconds at 13,200 rpm on a benchtop
612 centrifuge before adding one volume of chloroform. The mixture was further centrifuged
613 at 13,200 rpm for 60 seconds, after which 3X volume of water was added and the
614 mixture was vortexed before further centrifugation at 13,200 rpm for 60 seconds. The
615 upper aqueous layer was discarded while retaining the interface and the organic layer,
616 which was mixed with 3X volume of methanol, vortexed and centrifuged at 13,200 rpm
617 for 2 minutes. The supernatant was discarded, and the resulting pellet was dried and
618 resuspended in 0.1 M Tris containing 8M urea for further analysis of proteins by
619 immunoblotting.
620
621
622 **Immunoblotting**
623 Total cell lysates (10 µg) or purified 70S ribosomes (2.4 pmoles) were used for detecting
624 S13, MPY, Mrf-FLAG, and $S14_{C-}$, while 24 pmoles ribosome were used for detecting Rsh.
625 Samples were resolved on 8% SDS-PAGE (for FLAG, Rsh and GroEL analysis) or 12%
626 SDS-PAGE (for MPY, $S14_{C-}$ and S13), and proteins were probed with anti-FLAG (1:5000,
627 Genescript), anti-GroEL (1:5000, Enzo), anti-RelA (1:5000), anti-S13 of *E. coli* (1:100,
628 The Developmental Studies Hybridoma Bank), endogenously raised anti-MPY (1:5000)
629 and anti-$S14_{C-}$ (1:2000) antibodies.
630

631 **ppGpp extraction and analysis**

632 Cells of specified *M. smegmatis* strains were grown in Sauton's medium with either 1 mM
633 Zn or 1 μM TPEN for 96 hours, after which 1 mL of the culture was labelled with 100
634 μCi/mL of ^{32}P KH_2PO_4 (Perkin Elmer, 900-1100mCi/mmol) for 6 hours on a shaker at 37
635 ^{o}C. Labeled cells were washed once with TBST (20mM Tris pH7.6 + 150 mM NaCl +
636 0.05% Tween 80). Half of the cells (0.5 mL) were pelleted and resuspended in 25 μL of 4
637 M Formic acid (and kept frozen at -20 ^{o}C until ready for extraction). Remaining 0.5 mL
638 cells were starved for 3 hours in TBST, or metal-chelated TBST, or zinc-supplemented
639 TBST as specified. Following treatment, both pre- and post-starved cells were pelleted
640 and resuspended in 25 μL of 4 M formic acid and incubated on ice for 10 minutes. Cell
641 suspensions were frozen on dry ice for 10 minutes and thawed at 37 ^{o}C for 10 minutes.
642 The freeze-thaw cycle was repeated 5 times, after which the cell lysates were centrifuged
643 at 13,500 rpm for 5 minutes at 4 ^{o}C, and 5 μL of supernatants containing ^{32}P labeled
644 intracellular nucleotides were resolved on a 20 x 20 cm plastic PEI cellulose F TLC plate
645 (Millipore) using 1.5 M KH_2PO_4 pH 3.4 as a solvent. When the solvent front reached the
646 top of the plate, the plate was dried and exposed to X-ray film. 5 μL of 100 mM
647 nonradioactive nucleotides [ppGpp (Trilink), ATP, GDP and GTP (Thermo Fisher)] were
648 also resolved as positional markers, which were visualized by handheld UV lamp (Stuart,
649 Cole Palmer).

650

651 **Cryo-electron microscopy and image processing**

652 Quantifoil holey carbon copper grids R 1.2/1.3 were coated with a continuous layer of
653 carbon (~50 Å thick). After glow discharge for 30 s on a plasma sterilizer, 4 μl of the 200

654 nM Rsh-bound pre-elongation complex sample was placed on the grids. The sample
655 was incubated on the grids for 15 s at 4 °C and 100% humidity, followed by blotting for
656 4 s before flash-freezing into the liquid ethane using a Vitrobot IV (FEI). Data were
657 collected on a Titan Krios electron microscope at 300 keV using a K3 direct electron-
658 detecting camera (Gatan). −1.50 to −2.50 µm defocus range was used at a
659 magnification of 81,000×, yielding a pixel size of 0.846 Å. The dose rate of 23.3
660 electrons/pixel/second with a 2.05 second exposure time, with 41 frames of 0.05 second
661 duration each, resulted in a total dose of 66.59 e/Å−2. RELION 4.0 was used for data
662 processing. Image stacks were gain-corrected, dose-weighted, and aligned using
663 MotionCor2 (Zheng et al., 2017) for 9,103 micrographs. The contrast transfer function of
664 each aligned micrograph was estimated using CTFFIND-4.1 (Rohou and Grigorieff,
665 2015). A subset of micrographs was used for particle picking followed by 2D
666 classification. Relevant 2D classes were used for reference-based particle picking on all
667 micrographs yielding 1,928,609 particles. These particles were 2D classified and
668 suitable class averages selected (389,456 particles) (Fig. S7). The selected particles
669 were 3D refined and followed by 3D classification. Classes corresponding to
670 monosomes with 349,437 particles were selected for further processing. In order to
671 resolve structural heterogeneity in the monosome particles, we performed 3D
672 refinement using a large subunit mask followed by three rounds of fixed orientation 3D
673 classification. In the first round of fixed orientation 3D classification, we used an SSU
674 mask to resolve the SSU conformations into six classes. Class I with 158,489 particles
675 showed density corresponding to P-site tRNA and Rsh, representing the Rsh-bound
676 pre-elongation complex. We then performed the second round of fixed orientation 3D

classification on this class using a mask encompassing the entire inter-ribosomal subunit space such as the L7/L12-stalk, A-, P-, and E-site tRNA binding sites, and the L1-stalk regions. The second round of fixed orientation 3D classification resolved the conformational and particularly compositional heterogeneity in the masked region. We derived four classes with P-site tRNA density and two classes with P-site tRNA and Rsh densities. We performed the third round of fixed orientation 3D classification combining the two classes with P-site tRNA and Rsh densities, (49,058 particles) using a mask encompassing the P-site tRNA and Rsh. Two of the classes with a total of 36,321 particles showed significant density corresponding to P-site tRNA and Rsh. CTF refinement and Bayesian polishing of these particles yielded a map with a resolution of 2.7 Å.

Model building

Coordinates of the large and small subunits from our published C- *M. smegmatis* ribosome structure (PDB:6DZI) were docked as rigid bodies into the cryo-EM map using Chimera 1.14 (Pettersen et al., 2004). To achieve optimal fitting, we adjusted the model based on the densities in Coot (Emsley et al., 2010). The model was subsequently refined using PHENIX 1.14 (Adams et al., 2010). A predicted structure of *M. smegmatis* Rsh is available in the Alphafold Protein Structure database (Jumper et al., 2021). This structure was docked into the corresponding density in the cryo-EM map using Chimera 1.14 (Pettersen et al., 2004) and subsequently refined with Coot (Emsley *et al.*, 2010) and PHENIX 1.14 (Adams *et al.*, 2010). A validation report for the model was obtained from PHENIX 1.14 (Adams et al., 2010). The overall statistics of EM reconstruction and

molecular modeling are listed in Table S3. ChimeraX-1.0 (Pettersen et al., 2021) and Chimera 1.14 (Pettersen et al., 2004) were used to generate the structural figures in the manuscript.

Acknowledgments:

This work was supported by grants to AKO (NIH: AI132422, NIH: AI163599), CS (AI111696), RKA (NIH:GM61576), and YMH (NIH: GM134931). R.K.A. also acknowledges support to his lab through NIH R01 grants AI132422, GM139277 and AI155473. Support from the Wadsworth Center core facilities–Applied Genomic Technologies and the media core facility– is acknowledged. We also acknowledge Wadsworth Center's and New York Structural Biology Center's (NYSBC's) 3D-EM facilities. NYSBC EM facilities are supported by grants from the Simons Foundation (349247), NYSTAR, the NIH (GM103310) and the Agouron Institute (F00316). Authors acknowledge technical support from Kelley-Hurst, and discussions with Drs. Pallavi Ghosh, Keith Derbyshire and Todd Gray.

Authors' Contribution:

YL, RT, JC and AKO designed and performed genetics and biochemical experiments; SM, MRS, SRM, NKB and RKA designed and performed structural analysis and model construction; JP, CS, HG and YMH provided reagents. All authors wrote the manuscript.

Financial Conflict of Interest:

Authors declare no financial conflict of interest.

Data Deposition:

The cryo-EM map and atomic coordinates are being deposited in the Electron Microscopy and PDB Data Bank (wwPDB.org). Accession codes for these will be updated.

References

Adams, P.D., Afonine, P.V., Bunkoczi, G., Chen, V.B., Davis, I.W., Echols, N., Headd, J.J., Hung, L.W., Kapral, G.J., Grosse-Kunstleve, R.W., et al. (2010). PHENIX: a comprehensive Python-based system for macromolecular structure solution. Acta Crystallogr D Biol Crystallogr *66*, 213-221. 10.1107/S0907444909052925.

Andreini, C., Banci, L., Bertini, I., and Rosato, A. (2006). Zinc through the three domains of life. J Proteome Res *5*, 3173-3178. 10.1021/pr0603699.

Arenz, S., Abdelshahid, M., Sohmen, D., Payoe, R., Starosta, A.L., Berninghausen, O., Hauryliuk, V., Beckmann, R., and Wilson, D.N. (2016). The stringent factor RelA adopts an open conformation on the ribosome to stimulate ppGpp synthesis. Nucleic Acids Res *44*, 6471-6481. 10.1093/nar/gkw470.

Avarbock, A., Avarbock, D., Teh, J.S., Buckstein, M., Wang, Z.M., and Rubin, H. (2005). Functional regulation of the opposing (p)ppGpp synthetase/hydrolase activities of RelMtb from Mycobacterium tuberculosis. Biochemistry *44*, 9913-9923. 10.1021/bi0505316.

Avarbock, D., Avarbock, A., and Rubin, H. (2000). Differential regulation of opposing RelMtb activities by the aminoacylation state of a tRNA.ribosome.mRNA.RelMtb complex. Biochemistry *39*, 11640-11648. 10.1021/bi001256k.

Avarbock, D., Salem, J., Li, L.S., Wang, Z.M., and Rubin, H. (1999). Cloning and characterization of a bifunctional RelA/SpoT homologue from Mycobacterium tuberculosis. Gene *233*, 261-269. 10.1016/s0378-1119(99)00114-6.

Brown, A., Fernandez, I.S., Gordiyenko, Y., and Ramakrishnan, V. (2016). Ribosome-dependent activation of stringent control. Nature *534*, 277-280. 10.1038/nature17675.

Cashel, M., and Gallant, J. (1969). Two compounds implicated in the function of the RC gene of Escherichia coli. Nature *221*, 838-841. 10.1038/221838a0.

Chatterji, D., and Ojha, A.K. (2001). Revisiting the stringent response, ppGpp and starvation signaling. Curr Opin Microbiol *4*, 160-165. 10.1016/s1369-5274(00)00182-x.

Dahl, J.L., Kraus, C.N., Boshoff, H.I., Doan, B., Foley, K., Avarbock, D., Kaplan, G., Mizrahi, V., Rubin, H., and Barry, C.E., 3rd (2003). The role of RelMtb-mediated adaptation to stationary phase in long-term persistence of Mycobacterium tuberculosis in mice. Proc Natl Acad Sci U S A *100*, 10026-10031. 10.1073/pnas.1631248100.

Dalebroux, Z.D., and Swanson, M.S. (2012). ppGpp: magic beyond RNA polymerase. Nat Rev Microbiol *10*, 203-212. 10.1038/nrmicro2720.

Datta, P.P., Sharma, M.R., Qi, L., Frank, J., and Agrawal, R.K. (2005). Interaction of the G ' domain of elongation factor G and the C-terminal domain of ribosomal protein L7/L12 during translocation as revealed by cryo-EM. Molecular Cell *20*, 723-731. 10.1016/j.molcel.2005.10.028.

Diez, S., Ryu, J., Caban, K., Gonzalez, R.L., Jr., and Dworkin, J. (2020). The alarmones (p)ppGpp directly regulate translation initiation during entry into quiescence. Proc Natl Acad Sci U S A *117*, 15565-15572. 10.1073/pnas.1920013117.

Dutta, N.K., Klinkenberg, L.G., Vazquez, M.J., Segura-Carro, D., Colmenarejo, G., Ramon, F., Rodriguez-Miquel, B., Mata-Cantero, L., Porras-De Francisco, E., Chuang, Y.M., et al. (2019). Inhibiting the stringent response blocks Mycobacterium tuberculosis entry into quiescence and reduces persistence. Sci Adv *5*, eaav2104. 10.1126/sciadv.aav2104.

770 Ehrenstein, v. (1967). Isolation of sRNA from intact Escherichia coli cells. Methods in
771 Enzymology *12A*, 588-596.
772 Emsley, P., Lohkamp, B., Scott, W.G., and Cowtan, K. (2010). Features and development of Coot.
773 Acta Crystallogr D Biol Crystallogr *66*, 486-501. 10.1107/S0907444910007493.
774 English, B.P., Hauryliuk, V., Sanamrad, A., Tankov, S., Dekker, N.H., and Elf, J. (2011). Single-
775 molecule investigations of the stringent response machinery in living bacterial cells. Proc
776 Natl Acad Sci U S A *108*, E365-373. 10.1073/pnas.1102255108.
777 Friesen, J.D., Fiil, N.P., Parker, J.M., and Haseltine, W.A. (1974). A new relaxed mutant of
778 Escherichia coli with an altered 50S ribosomal subunit. Proc Natl Acad Sci U S A *71*, 3465-
779 3469. 10.1073/pnas.71.9.3465.
780 Gabashvili, I.S., Agrawal, R.K., Spahn, C.M., Grassucci, R.A., Svergun, D.I., Frank, J., and Penczek,
781 P. (2000). Solution structure of the E. coli 70S ribosome at 11.5 A resolution. Cell *100*,
782 537-549. 10.1016/s0092-8674(00)80690-x.
783 Gamper, H., and Hou, Y.M. (2020). A Label-Free Assay for Aminoacylation of tRNA. Genes (Basel)
784 *11*. 10.3390/genes11101173.
785 Gao, X., Yeom, J., and Groisman, E.A. (2019). The expanded specificity and physiological role of
786 a widespread N-degron recognin. Proc Natl Acad Sci U S A *116*, 18629-18637.
787 10.1073/pnas.1821060116.
788 Gohara, D.W., and Yap, M.F. (2018). Survival of the drowsiest: the hibernating 100S ribosome
789 in bacterial stress management. Curr Genet *64*, 753-760. 10.1007/s00294-017-0796-2.
790 Gratani, F.L., Horvatek, P., Geiger, T., Borisova, M., Mayer, C., Grin, I., Wagner, S., Steinchen,
791 W., Bange, G., Velic, A., et al. (2018). Regulation of the opposing (p)ppGpp synthetase
792 and hydrolase activities in a bifunctional RelA/SpoT homologue from Staphylococcus
793 aureus. PLoS Genet *14*, e1007514. 10.1371/journal.pgen.1007514.
794 Gropp, M., Strausz, Y., Gross, M., and Glaser, G. (2001). Regulation of Escherichia coli RelA
795 requires oligomerization of the C-terminal domain. J Bacteriol *183*, 570-579.
796 10.1128/JB.183.2.570-579.2001.
797 Hogg, T., Mechold, U., Malke, H., Cashel, M., and Hilgenfeld, R. (2004). Conformational
798 antagonism between opposing active sites in a bifunctional RelA/SpoT homolog
799 modulates (p)ppGpp metabolism during the stringent response [corrected]. Cell *117*,
800 57-68. 10.1016/s0092-8674(04)00260-0.
801 Hood, R.D., Higgins, S.A., Flamholz, A., Nichols, R.J., and Savage, D.F. (2016). The stringent
802 response regulates adaptation to darkness in the cyanobacterium Synechococcus
803 elongatus. Proc Natl Acad Sci U S A *113*, E4867-4876. 10.1073/pnas.1524915113.
804 Hu, Y., and Liu, B. (2022). Roles of zinc-binding domain of bacterial RNA polymerase in
805 transcription. Trends Biochem Sci *47*, 710-724. 10.1016/j.tibs.2022.03.007.
806 Irving, S.E., Choudhury, N.R., and Corrigan, R.M. (2021). The stringent response and
807 physiological roles of (pp)pGpp in bacteria. Nat Rev Microbiol *19*, 256-271.
808 10.1038/s41579-020-00470-y.
809 Izutsu, K., Wada, A., and Wada, C. (2001). Expression of ribosome modulation factor (RMF) in
810 Escherichia coli requires ppGpp. Genes Cells *6*, 665-676. 10.1046/j.1365-
811 2443.2001.00457.x.

812 Jain, V., Saleem-Batcha, R., China, A., and Chatterji, D. (2006). Molecular dissection of the
813 mycobacterial stringent response protein Rel. Protein Sci *15*, 1449-1464.
814 10.1110/ps.062117006.
815 Jumper, J., Evans, R., Pritzel, A., Green, T., Figurnov, M., Ronneberger, O., Tunyasuvunakool, K.,
816 Bates, R., Zidek, A., Potapenko, A., et al. (2021). Highly accurate protein structure
817 prediction with AlphaFold. Nature *596*, 583-589. 10.1038/s41586-021-03819-2.
818 Kudrin, P., Dzhygyr, I., Ishiguro, K., Beljantseva, J., Maksimova, E., Oliveira, S.R.A., Varik, V.,
819 Payoe, R., Konevega, A.L., Tenson, T., et al. (2018). The ribosomal A-site finger is crucial
820 for binding and activation of the stringent factor RelA. Nucleic Acids Res *46*, 1973-1983.
821 10.1093/nar/gky023.
822 Lai, R.P.J., Cortes, T., Marais, S., Rockwood, N., Burke, M.L., Garza-Garcia, A., Horswell, S., Sesay,
823 A.K., O'Garra, A., Young, D.B., and Wilkinson, R.J. (2021). Transcriptomic
824 Characterization of Tuberculous Sputum Reveals a Host Warburg Effect and Microbial
825 Cholesterol Catabolism. mBio *12*, e0176621. 10.1128/mBio.01766-21.
826 Li, Y., Corro, J.H., Palmer, C.D., and Ojha, A.K. (2020). Progression from remodeling to
827 hibernation of ribosomes in zinc-starved mycobacteria. Proc Natl Acad Sci U S A *117*,
828 19528-19537. 10.1073/pnas.2013409117.
829 Li, Y., Keshavan, P., Corro, J.H., Koripella, R.K., Agrawal, R.K., and Ojha, A.K. (2021a). Purification
830 of Hibernating and Active C- Ribosomes from Zinc-Starved Mycobacteria. Methods Mol
831 Biol *2314*, 151-166. 10.1007/978-1-0716-1460-0_5.
832 Li, Y., Sharma, M.R., Koripella, R.K., Banavali, N.K., Agrawal, R.K., and Ojha, A.K. (2021b).
833 Ribosome hibernation: a new molecular framework for targeting nonreplicating
834 persisters of mycobacteria. Microbiology (Reading) *167*. 10.1099/mic.0.001035.
835 Li, Y., Sharma, M.R., Koripella, R.K., Yang, Y., Kaushal, P.S., Lin, Q., Wade, J.T., Gray, T.A.,
836 Derbyshire, K.M., Agrawal, R.K., and Ojha, A.K. (2018). Zinc depletion induces ribosome
837 hibernation in mycobacteria. Proc Natl Acad Sci U S A *115*, 8191-8196.
838 10.1073/pnas.1804555115.
839 Loveland, A.B., Bah, E., Madireddy, R., Zhang, Y., Brilot, A.F., Grigorieff, N., and Korostelev, A.A.
840 (2016). Ribosome*RelA structures reveal the mechanism of stringent response
841 activation. Elife *5*. 10.7554/eLife.17029.
842 Marshall, R.A., Aitken, C.E., and Puglisi, J.D. (2009). GTP hydrolysis by IF2 guides progression of
843 the ribosome into elongation. Mol Cell *35*, 37-47. 10.1016/j.molcel.2009.06.008.
844 Mechold, U., Murphy, H., Brown, L., and Cashel, M. (2002). Intramolecular regulation of the
845 opposing (p)ppGpp catalytic activities of Rel(Seq), the Rel/Spo enzyme from
846 Streptococcus equisimilis. J Bacteriol *184*, 2878-2888. 10.1128/JB.184.11.2878-
847 2888.2002.
848 Ojha, A.K., Mukherjee, T.K., and Chatterji, D. (2000). High intracellular level of guanosine
849 tetraphosphate in Mycobacterium smegmatis changes the morphology of the
850 bacterium. Infect Immun *68*, 4084-4091. 10.1128/IAI.68.7.4084-4091.2000.
851 Parker, J., Watson, R.J., and Friesen, J.D. (1976). A relaxed mutant with an altered ribosomal
852 protein L11. Mol Gen Genet *144*, 111-114. 10.1007/BF00277313.
853 Pausch, P., Abdelshahid, M., Steinchen, W., Schafer, H., Gratani, F.L., Freibert, S.A., Wolz, C.,
854 Turgay, K., Wilson, D.N., and Bange, G. (2020). Structural Basis for Regulation of the

855 Opposing (p)ppGpp Synthetase and Hydrolase within the Stringent Response
856 Orchestrator Rel. Cell Rep *32*, 108157. 10.1016/j.celrep.2020.108157.
857 Pettersen, E.F., Goddard, T.D., Huang, C.C., Couch, G.S., Greenblatt, D.M., Meng, E.C., and
858 Ferrin, T.E. (2004). UCSF Chimera--a visualization system for exploratory research and
859 analysis. J Comput Chem *25*, 1605-1612. 10.1002/jcc.20084.
860 Pettersen, E.F., Goddard, T.D., Huang, C.C., Meng, E.C., Couch, G.S., Croll, T.I., Morris, J.H., and
861 Ferrin, T.E. (2021). UCSF ChimeraX: Structure visualization for researchers, educators,
862 and developers. Protein Sci *30*, 70-82. 10.1002/pro.3943.
863 Pletzer, D., Blimkie, T.M., Wolfmeier, H., Li, Y., Baghela, A., Lee, A.H.Y., Falsafi, R., and Hancock,
864 R.E.W. (2020). The Stringent Stress Response Controls Proteases and Global Regulators
865 under Optimal Growth Conditions in Pseudomonas aeruginosa. mSystems *5*.
866 10.1128/mSystems.00495-20.
867 Potrykus, K., and Cashel, M. (2008). (p)ppGpp: still magical? Annu Rev Microbiol *62*, 35-51.
868 10.1146/annurev.micro.62.081307.162903.
869 Primm, T.P., Andersen, S.J., Mizrahi, V., Avarbock, D., Rubin, H., and Barry, C.E., 3rd (2000). The
870 stringent response of Mycobacterium tuberculosis is required for long-term survival. J
871 Bacteriol *182*, 4889-4898. 10.1128/JB.182.17.4889-4898.2000.
872 Prisic, S., Hwang, H., Dow, A., Barnaby, O., Pan, T.S., Lonzanida, J.A., Chazin, W.J., Steen, H., and
873 Husson, R.N. (2015). Zinc regulates a switch between primary and alternative S18
874 ribosomal proteins in Mycobacterium tuberculosis. Mol Microbiol *97*, 263-280.
875 10.1111/mmi.13022.
876 Prossliner, T., Skovbo Winther, K., Sorensen, M.A., and Gerdes, K. (2018). Ribosome
877 Hibernation. Annu Rev Genet *52*, 321-348. 10.1146/annurev-genet-120215-035130.
878 Prusa, J., Zhu, D.X., and Stallings, C.L. (2018). The stringent response and Mycobacterium
879 tuberculosis pathogenesis. Pathog Dis *76*. 10.1093/femspd/fty054.
880 Richards, J.P., Cai, W., Zill, N.A., Zhang, W., and Ojha, A.K. (2019). Adaptation of Mycobacterium
881 tuberculosis to Biofilm Growth Is Genetically Linked to Drug Tolerance. Antimicrob
882 Agents Chemother *63*. 10.1128/AAC.01213-19.
883 Rohou, A., and Grigorieff, N. (2015). CTFFIND4: Fast and accurate defocus estimation from
884 electron micrographs. J Struct Biol *192*, 216-221. 10.1016/j.jsb.2015.08.008.
885 Ronneau, S., Caballero-Montes, J., Coppine, J., Mayard, A., Garcia-Pino, A., and Hallez, R. (2019).
886 Regulation of (p)ppGpp hydrolysis by a conserved archetypal regulatory domain. Nucleic
887 Acids Res *47*, 843-854. 10.1093/nar/gky1201.
888 Ross, W., Vrentas, C.E., Sanchez-Vazquez, P., Gaal, T., and Gourse, R.L. (2013). The magic spot:
889 a ppGpp binding site on E. coli RNA polymerase responsible for regulation of
890 transcription initiation. Mol Cell *50*, 420-429. 10.1016/j.molcel.2013.03.021.
891 Sankaranarayanan, R., Dock-Bregeon, A.C., Romby, P., Caillet, J., Springer, M., Rees, B.,
892 Ehresmann, C., Ehresmann, B., and Moras, D. (1999). The structure of threonyl-tRNA
893 synthetase-tRNA(Thr) complex enlightens its repressor activity and reveals an essential
894 zinc ion in the active site. Cell *97*, 371-381. 10.1016/s0092-8674(00)80746-1.
895 Schafer, H., Beckert, B., Frese, C.K., Steinchen, W., Nuss, A.M., Beckstette, M., Hantke, I., Driller,
896 K., Sudzinova, P., Krasny, L., et al. (2020). The alarmones (p)ppGpp are part of the heat
897 shock response of Bacillus subtilis. PLoS Genet *16*, e1008275.
898 10.1371/journal.pgen.1008275.

899 Sprink, T., Ramrath, D.J., Yamamoto, H., Yamamoto, K., Loerke, J., Ismer, J., Hildebrand, P.W.,
900 Scheerer, P., Burger, J., Mielke, T., and Spahn, C.M. (2016). Structures of ribosome-
901 bound initiation factor 2 reveal the mechanism of subunit association. Sci Adv *2*,
902 e1501502. 10.1126/sciadv.1501502.
903 Stallings, C.L., Stephanou, N.C., Chu, L., Hochschild, A., Nickels, B.E., and Glickman, M.S. (2009).
904 CarD is an essential regulator of rRNA transcription required for Mycobacterium
905 tuberculosis persistence. Cell *138*, 146-159. 10.1016/j.cell.2009.04.041.
906 Takada, H., Roghanian, M., Caballero-Montes, J., Van Nerom, K., Jimmy, S., Kudrin, P., Trebini,
907 F., Murayama, R., Akanuma, G., Garcia-Pino, A., and Hauryliuk, V. (2021). Ribosome
908 association primes the stringent factor Rel for tRNA-dependent locking in the A-site and
909 activation of (p)ppGpp synthesis. Nucleic Acids Res *49*, 444-457. 10.1093/nar/gkaa1187.
910 Takada, H., Roghanian, M., Murina, V., Dzhygyr, I., Murayama, R., Akanuma, G., Atkinson, G.C.,
911 Garcia-Pino, A., and Hauryliuk, V. (2020). The C-Terminal RRM/ACT Domain Is Crucial for
912 Fine-Tuning the Activation of 'Long' RelA-SpoT Homolog Enzymes by Ribosomal
913 Complexes. Front Microbiol *11*, 277. 10.3389/fmicb.2020.00277.
914 Tamman, H., Van Nerom, K., Takada, H., Vandenberk, N., Scholl, D., Polikanov, Y., Hofkens, J.,
915 Talavera, A., Hauryliuk, V., Hendrix, J., and Garcia-Pino, A. (2020). A nucleotide-switch
916 mechanism mediates opposing catalytic activities of Rel enzymes. Nat Chem Biol *16*,
917 834-840. 10.1038/s41589-020-0520-2.
918 Turnbull, K.J., Dzhygyr, I., Lindemose, S., Hauryliuk, V., and Roghanian, M. (2019).
919 Intramolecular Interactions Dominate the Autoregulation of Escherichia coli Stringent
920 Factor RelA. Front Microbiol *10*, 1966. 10.3389/fmicb.2019.01966.
921 Vilcheze, C., and Jacobs, W.R., Jr. (2019). The Isoniazid Paradigm of Killing, Resistance, and
922 Persistence in Mycobacterium tuberculosis. J Mol Biol *431*, 3450-3461.
923 10.1016/j.jmb.2019.02.016.
924 Weiss, L.A., and Stallings, C.L. (2013). Essential roles for Mycobacterium tuberculosis Rel beyond
925 the production of (p)ppGpp. J Bacteriol *195*, 5629-5638. 10.1128/JB.00759-13.
926 Wendrich, T.M., Blaha, G., Wilson, D.N., Marahiel, M.A., and Nierhaus, K.H. (2002). Dissection
927 of the mechanism for the stringent factor RelA. Mol Cell *10*, 779-788. 10.1016/s1097-
928 2765(02)00656-1.
929 Winther, K.S., Roghanian, M., and Gerdes, K. (2018). Activation of the Stringent Response by
930 Loading of RelA-tRNA Complexes at the Ribosomal A-Site. Mol Cell *70*, 95-105 e104.
931 10.1016/j.molcel.2018.02.033.
932 Yang, X., and Ishiguro, E.E. (2001). Involvement of the N terminus of ribosomal protein L11 in
933 regulation of the RelA protein of Escherichia coli. J Bacteriol *183*, 6532-6537.
934 10.1128/JB.183.22.6532-6537.2001.
935 Yokoyama, T., Shaikh, T.R., Iwakura, N., Kaji, H., Kaji, A., and Agrawal, R.K. (2012). Structural
936 insights into initial and intermediate steps of the ribosome-recycling process. Embo J *31*,
937 1836-1846. 10.1038/emboj.2012.22.
938 Zheng, S.Q., Palovcak, E., Armache, J.P., Verba, K.A., Cheng, Y., and Agard, D.A. (2017).
939 MotionCor2: anisotropic correction of beam-induced motion for improved cryo-
940 electron microscopy. Nat Methods *14*, 331-332. 10.1038/nmeth.4193.
941
942

Starvation sensing by mycobacterial RelA/SpoT homologue

A

NTD
CTD
HYD
SYN
TGS
AHD
ZBD
ACT
RelA/Rsh

B

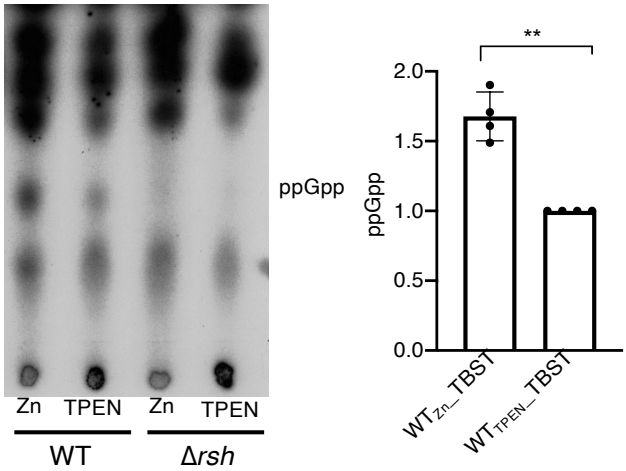
ppGpp
Zn
TPEN
Zn
TPEN
WT
Δrsh
**
2.0
1.5
1.0
0.5
0.0
ppGpp
WTZn_TBST
WTTPEN_TBST

C

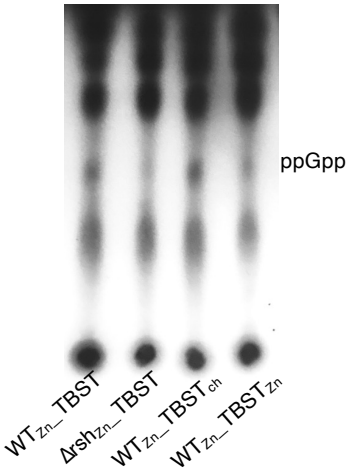
ppGpp
WTZn_TBST
ΔrshZn_TBST
WTZn_TBSTch
WTZn_TBSTZn

D

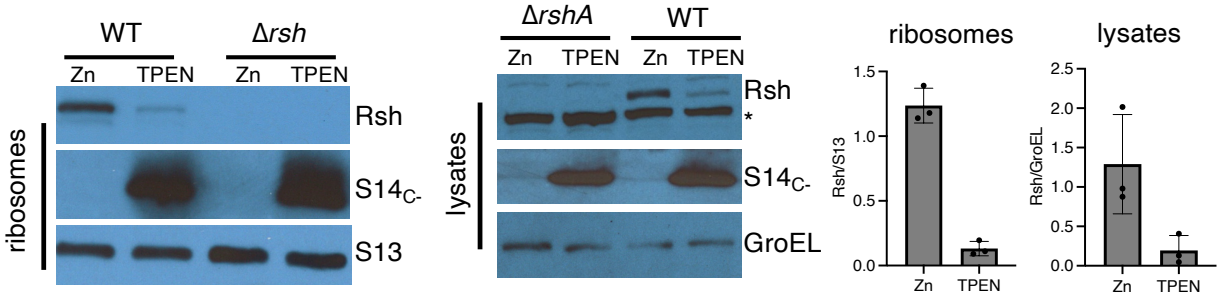
WT
Δrsh
Zn
TPEN
Zn
TPEN
ribosomes
Rsh
S14C-
S13
ΔrshA
WT
Zn
TPEN
Zn
TPEN
lysates
Rsh
*
S14C-
GroEL
ribosomes
lysates
Rsh/S13
Rsh/GroEL
1.5
1.0
0.5
0.0
2.5
2.0
1.5
1.0
0.5
0.0
Zn
TPEN
Zn
TPEN

Figure 1: Attenuated stringent response and loss of Rsh in zinc-starved mycobacteria. A. Domain architecture of *E. coli* RelA or mycobacterial RelA/SpoT homologue (Rsh). The N-terminal domain (NTD) containing the hydrolase (HYD) and synthase (SYN) is separated from the C-terminal domain (CTD) by TGS (Thr-RS, GTPase and SpoT) and alpha-helix domain (AHD). The CTD is comprised of ZBD (zinc binding domain) and ACT (aspartokinase, chorismate mutase and TyrA) subdomains. **B.** Radio-TLC showing ppGpp levels in cultures of *M. smegmatis* wildtype (WT) from high-zinc (1mM $ZnSO_4$) and low-zinc (1 μM TPEN) Sauton's medium after 96 hours of growth. ^{32}P-labeled sodium phosphate (10 **µ**Ci/mL) was added to the cultures six hours prior to starvation, after which nucleotides were extracted in formic acid and amounts equivalent to 50000 cpm were analyzed by TLC. Purified cold ppGpp was loaded as positional marker. The plot shows quantitative analysis of the ppGpp levels in high-zinc WT samples relative to their low-zinc counterparts from four biologically independent experiments. **C.** Radio-TLC showing ppGpp levels in WT cells cultured for 96-hours in high-zinc Sauton's medium, then labelled for six hours, and resuspended in either TBST, or Chelex-100 treated TBST ($TBST_{ch}$), or zinc-supplemented $TBST_{ch}$ ($TBST_{Zn}$). Δ*rsh* mutant was analyzed as control in panels B and C. **D**. Immunoblot analysis of Rsh levels in 70S ribosomes purified from 96-hour-old high-and low-zinc cultures of *M. smegmatis* strains described in panel B. S14c- was probed for the remodeled C- ribosome, while S13 was probed as the loading control. In the set of immunoblots on the right, cell lysates from the samples used for ribosome analysis were probed. The asterisk indicates a non-specific unknown protein cross-reactive to Rsh antibody. The plots to the extreme right show normalized average difference in Rsh between high- and low-zinc cultures from three independent experiments.

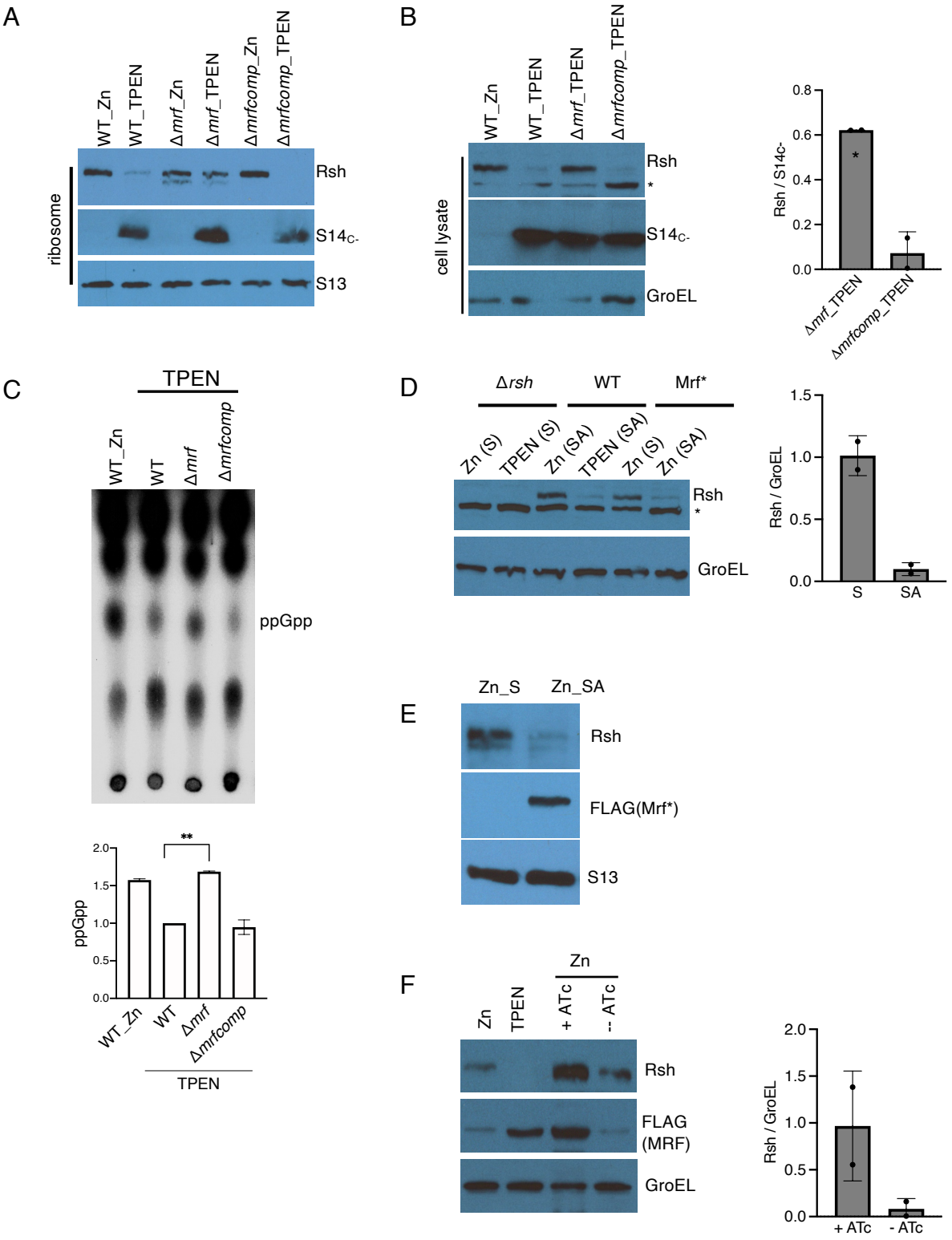
A
WT_Zn
WT_TPEN
Δmrf_Zn
Δmrf_TPEN
Δmrfcomp_Zn
Δmrfcomp_TPEN
ribosome
Rsh
S14c-
S13
B
WT_Zn
WT_TPEN
Δmrf_TPEN
Δmrfcomp_TPEN
cell lysate
Rsh
*
S14c-
GroEL
Rsh / S14c-
0.8
0.6
0.4
0.2
0.0
*
Δmrf_TPEN
Δmrfcomp_TPEN
C
TPEN
WT_Zn
WT
Δmrf
Δmrfcomp
ppGpp
ppGpp
2.0
1.5
1.0
0.5
0.0
**
WT_Zn
WT
Δmrf
Δmrfcomp
TPEN
D
Δrsh
WT
Mrf*
Zn (S)
TPEN (S)
Zn (SA)
TPEN (SA)
Zn (S)
Zn (SA)
Rsh
*
GroEL
Rsh / GroEL
1.5
1.0
0.5
0.0
S
SA
E
Zn_S
Zn_SA
Rsh
FLAG(Mrf*)
S13
F
Zn
Zn
TPEN
+ ATc
-- ATc
Rsh
FLAG
(MRF)
GroEL
Rsh / GroEL
2.0
1.5
1.0
0.5
0.0
+ ATc
- ATc

Figure 2: Mrf accumulation causes loss of Rsh. A-B. Analysis of Rsh in 70S ribosomes (B) and cell lysates (C) from high- or low-zinc cultures of Δ*mrf* and complemented (Δ*mrf*comp) strains of *M. smegmatis.* High and low-zinc cultures of WT were controls. $S14_{c-}$, S13 and GroEL were probed as loading controls for ribosomes or cell lysates as indicated. The asterisk in panel B indicates a non-specific protein cross-reactive to Rsh antibody. **C.** Radio-TLC showing ppGpp levels in 96-hour old high- or low-zinc cultures of WT and low-zinc cultures of Δ*mrf and* Δ*mrfcomp* of *M. smegmatis* strains after 3-hours of starvation in TBST medium. Purified cold ppGpp was loaded as positional marker. The plot shows quantitative analysis of the relative ppGpp levels in each sample compared to the level in WT_TPEN culture from two biologically independent experiments. **D.** Ectopic Mrf accumulation causes loss of Rsh. Levels of Rsh in the cell lysates of a *M. smegmatis* strain (pYL222) expressing FLAG-Tagged Mrf* under the acetamide-inducible promoter. Cells were cultured in high-zinc Sauton's medium (1mM ZnSO4; denoted Zn) containing 0.2% succinate (denoted S) as the carbon source until OD 0.6, after which Mrf* expression was induced with 0.2% acetamide (denoted SA), and cells were grown for 96 hours from inoculation. Uninduced cells (S) were used as the reference. As controls, 96-hour old cells from the wildtype (WT) and Δ*rsh* strains cultured in either high- or low-zinc (1μM TPEN) Sauton's medium with succinate (S) or succinate + acetamide-induced (SA) conditions, as indicated. The plot shows average normalized density of Rsh from two independent experiments. **E.** Analysis of Rsh in ribosomes purified from 96-hour-old induced (SA) or uninduced (S) high-zinc cultures of pYL222 strain. **F.** Simultaneous accumulation of Rsh and Mrf in YL9 cells (Li et al. 2020) upon conditional depletion of ClpP1 protease (lane 3). Cells were grown in high-zinc Sauton's medium until OD of 0.6, after which anhydrotetracycline (Atc) was added to induce CRISPRi system to deplete ClpP1. Cell lysates were analyzed after 16 hours of ClpP1 depletion. A parallel uninduced cells were used as control (lane 4). YL9 cells grown for 96 hours in high- or low-zinc Sauton's medium without ATc (lane 1 and 2, respectively) were used as reference. The plot shows average normalized density of Rsh from two independent experiments.

A

```
Ec_RelA     QNRSKDNGRVVVEGVGNLMHHIARCCQPIPGDEIVGFITQGRGISVHRADCEQLAELRSH  647
Mtb_Rsh     RPRSTDDVGVSVPGAPGVLTKLAKCCTPVPGDVIMGFVTRGGGVSVHRTDCTNAASLQQ-  693
Msm_Rsh     RQRSNDDTGVAVPGAPGVLTKLAKCCTPVPGDTIMGFVTRGGGVSVHRTDCTNAESLQQ-  700
```

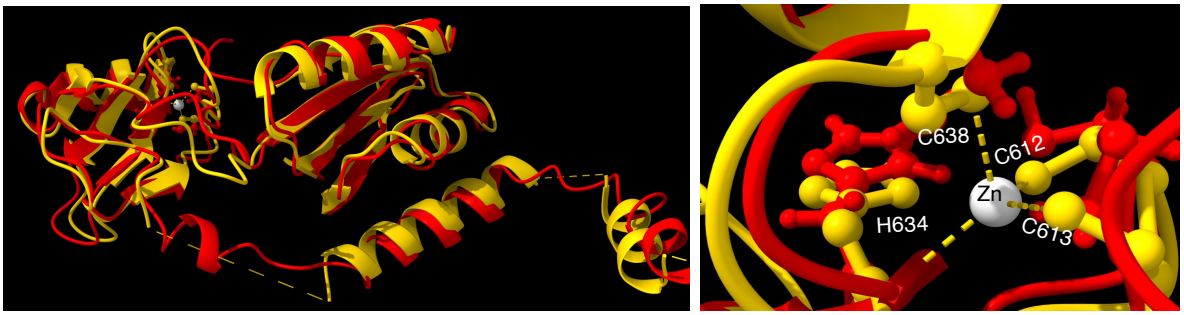

B

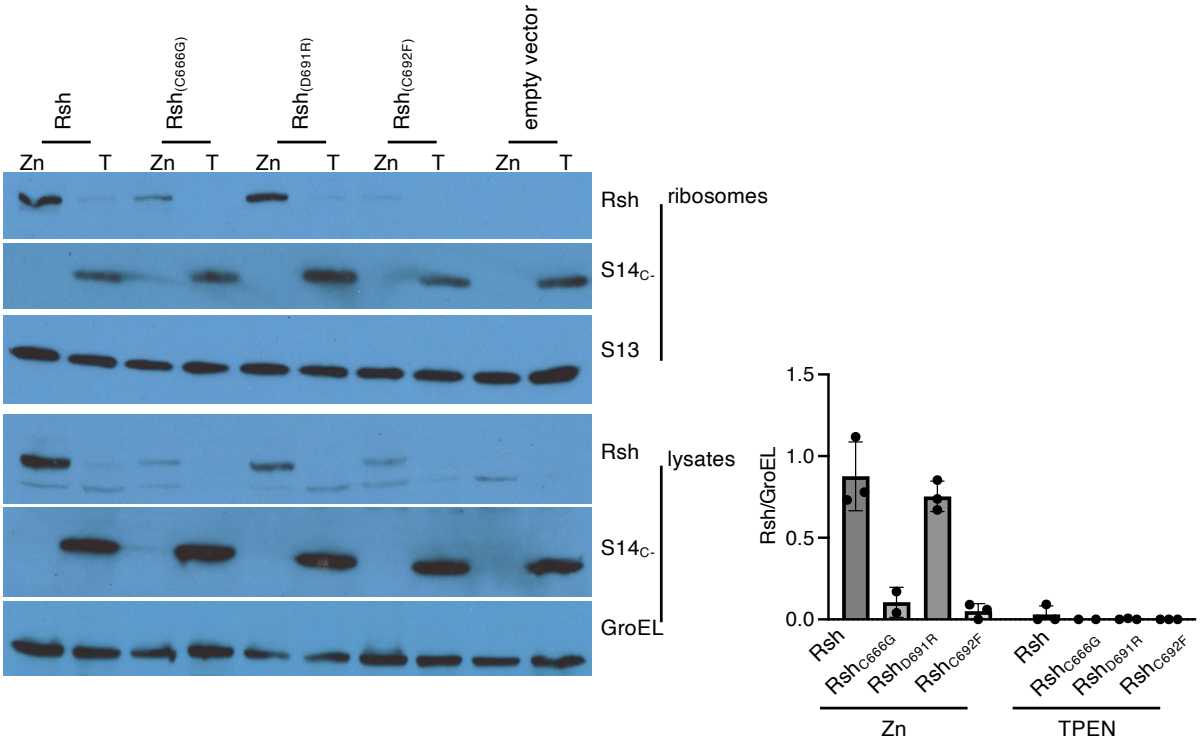

C

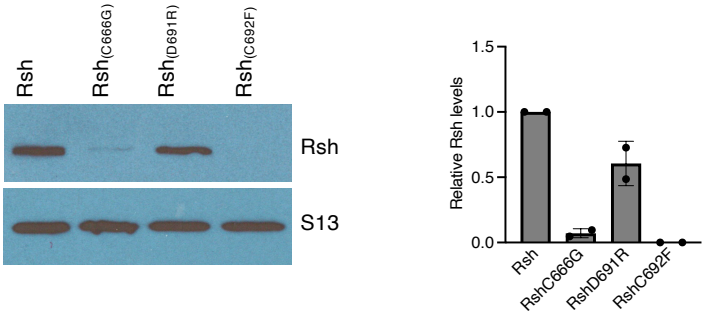

Figure 3: **Ribosome binding residues in Rsh are critical for its intracellular stability**. **A.** (Top) Sequence alignment of the C- terminal region of Rsh from *E. coli*, *M. smegmatis* and *M. tuberculosis* depicting the CCHC like zinc-finger (highlighted yellow) in the ZBD of Rsh. (Bottom) Superimposition of the structure (PDBID: 5IQR) of the ZBD region from *E. coli* and *M. smegmatis* (red). Zinc atom coordinated (shown with dashed lines) by the CCHC motif (shown as ball-and-stick model and numbered based on *E. coli* sequence) has been zoomed in the image to the right. The corresponding residues from *M. smegmatis* (shown in red ball-and-stick model) predict similarity in spatial orientation with respect to their *E. coli* counterparts. **B.** Immunoblot analysis of Rsh variants ($C_{666}G$, $D_{691}R$ and $C_{692}F$) in cell lysates and 70S ribosomes purified from 96-hour-old high-zinc cultures of a Δ*rsh* strain *of M. smegmatis* expressing each Rsh variant individually from an integrative plasmid (pYL238, pYL240, pYL241, pYL242 for Rsh, Rsh_{C666G}, Rsh_{D691R} and Rsh_{C692F}, respectively). Cultures of Δ*rsh* strain expressing WT RSH were controls. Normalized average levels of Rsh and its variants in cell lysates from three independent experiments are shown in the plot. **C.** *In vitro* ribosome binding of recombinant Rsh and its variants. 2.4 picomoles of 70S ribosomes purified from a 96-hour old high-zinc culture of Δ*rsh* strain of *M. smegmatis* were mixed with 1.2 picomoles of Rsh or variant proteins (purified from recombinant *E. coli* harboring pYL243, pYL246, pYL247, pY248 for Rsh, Rsh_{C666F}, Rsh_{D691R} and Rsh_{C692F}, respectively) and the mixture was incubated for 30 minutes at 37 °C. The complex was separated by ultracentrifugation through a 32% sucrose cushion. S13 was probed as the loading control. The plot shows quantitative analysis of Rsh from two biologically independent experiments.

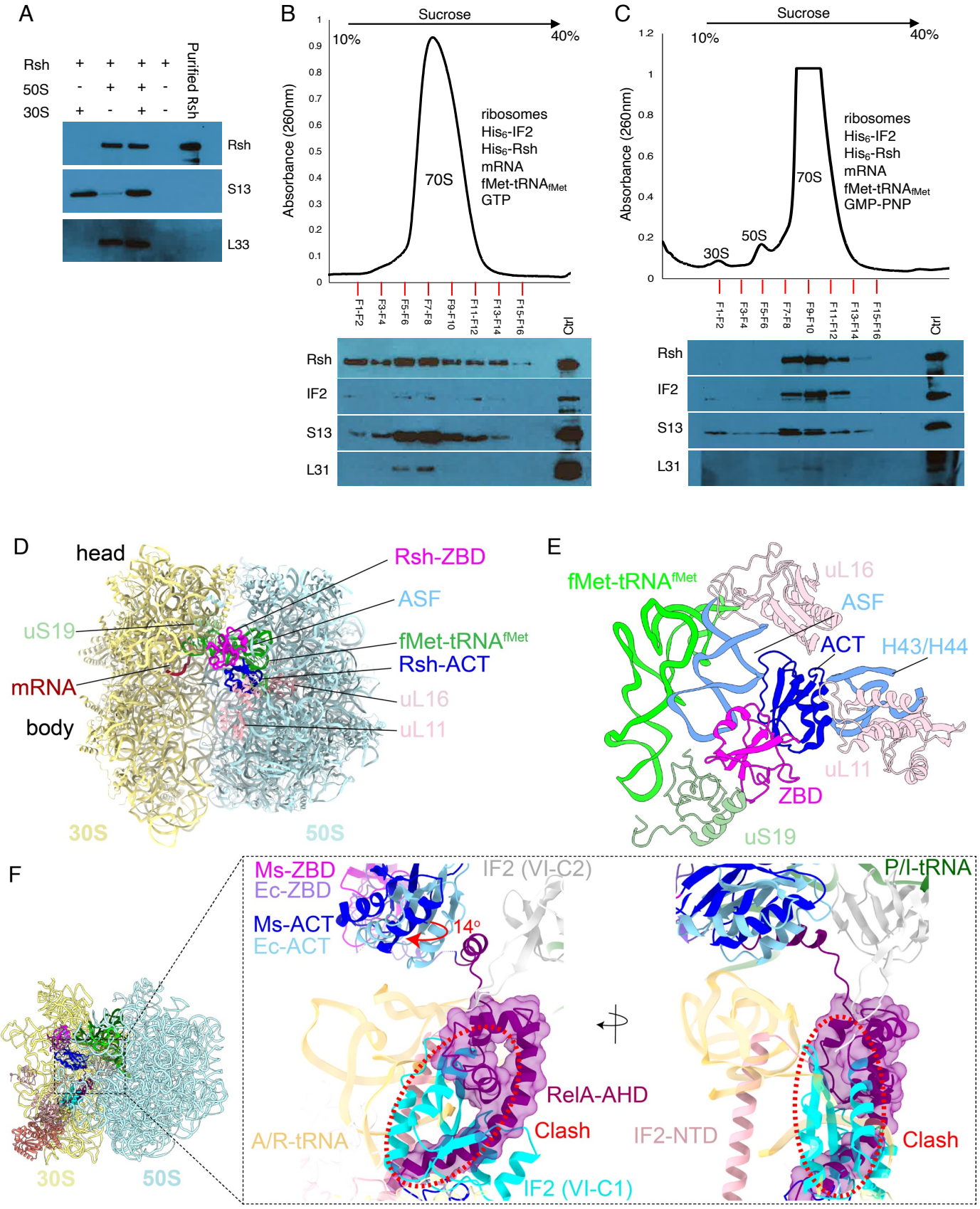
A
Rsh
50S
30S
Purified Rsh
Rsh
S13
L33
B
Sucrose
10%
40%
Absorbance (260nm)
70S
ribosomes
His6-IF2
His6-Rsh
mRNA
fMet-tRNAfMet
GTP
F1-F2
F3-F4
F5-F6
F7-F8
F9-F10
F11-F12
F13-F14
F15-F16
Ctrl
Rsh
IF2
S13
L31
C
Sucrose
10%
40%
Absorbance (260nm)
70S
50S
30S
ribosomes
His6-IF2
His6-Rsh
mRNA
fMet-tRNAfMet
GMP-PNP
F1-F2
F3-F4
F5-F6
F7-F8
F9-F10
F11-F12
F13-F14
F15-F16
Ctrl
Rsh
IF2
S13
L31
D
head
Rsh-ZBD
ASF
uS19
fMet-tRNAfMet
Rsh-ACT
mRNA
uL16
body
uL11
30S
50S
E
fMet-tRNAfMet
uL16
ASF
ACT
H43/H44
uL11
ZBD
uS19
F
30S
50S
Ms-ZBD
Ec-ZBD
IF2 (VI-C2)
Ms-ACT
Ec-ACT
14º
P/I-tRNA
RelA-AHD
Clash
A/R-tRNA
IF2-NTD
Clash
IF2 (VI-C1)

Figure 4: **Rsh interaction with a 70S translation initiation complex. A.** Co-sedimentation of Rsh with the 50S ribosomal subunit. Pellets resulting from centrifugation on a 32% sucrose cushion were analyzed for S13 to confirm small subunit, $L33_{C-}$ to confirm large subunit, and Rsh to test preferential subunit binding. Rsh in the absence of ribosomes was included as control to rule out sedimentation of free protein. Purified Rsh was loaded as marker. **B-C.** Reconstitution of Rsh-bound pre-elongation complex in the presence of GTP (B) or GMP-PNP (C). Dissociated ribosomes (Figure S6) were mixed with indicated ligands in the presence of GTP or GMPPNP. After incubation for 15 minutes in low-magnesium (1mM $MgCl_2$) buffer, recombinant Rsh was added, and magnesium was adjusted to 10 mM. The resulting mixture was incubated for additional 30 minutes. The complex was resolved in 10-40% SDG, and fractions corresponding to 70S-peak and its margin were analyzed for Rsh, IF2 and indicated ribosomal proteins by immunoblotting using anti-Rsh, anti-His_6 (for IF2), anti-S13 and anti-L31 antibodies. All reagents in the reactions in panels C and D were added in 5-fold molar excess relative to the ribosomal subunits. **D.** 2.7 Å resolution cryo-EM structure of the 70S-Rsh complex in pre-elongation state of translation, with a fMet-$tRNA_i^{Met}$ present in the P-site (green), mRNA (brown), and Rsh' two C-terminal domains, ZBD (magenta) and ACT (blue). The 30S and 50S subunits are shown in yellow and blue, respectively. **E**. Ribosomal components interacting with Rsh ZBD and ACT domain, along with the fMet-$tRNA_f^{Met}$ in the P-site (green), are shown. ZBD interacts with components of inter-subunit bridge B1a, uS19 (light green), and the A-site finger (ASF, sky blue). ACT interacts with the 50S components uL16 (sky blue), L11, and 23S rRNA helices H43/44 (sky blue). **F.** Superimposition of *M. smegmatis* 70S-Rsh, *E. coli* 70S-RelA (PDB ID: 5KPV) and *E. coli* 70S-IF2 (PDB ID: 6HTQ) structures, comparing their binding sites and conformations on the ribosome. Position of IF2 (VI-C1, cyan) suggests a direct steric clash (highlighted by red dotted circle) with the *E. coli* RelA's α-helical domain (RelA-AHD, purple). *M. smegmatis* Rsh-ACT (Ms-ACT, blue) is rotated by ~14° (indicated by a red arrow) relative to the *E. coli* RelA-ACT (Ec-ACT, light blue), while the ZBD domains (Ms-ZBD, magenta and Ec-ZBD in light purple) have the same position.

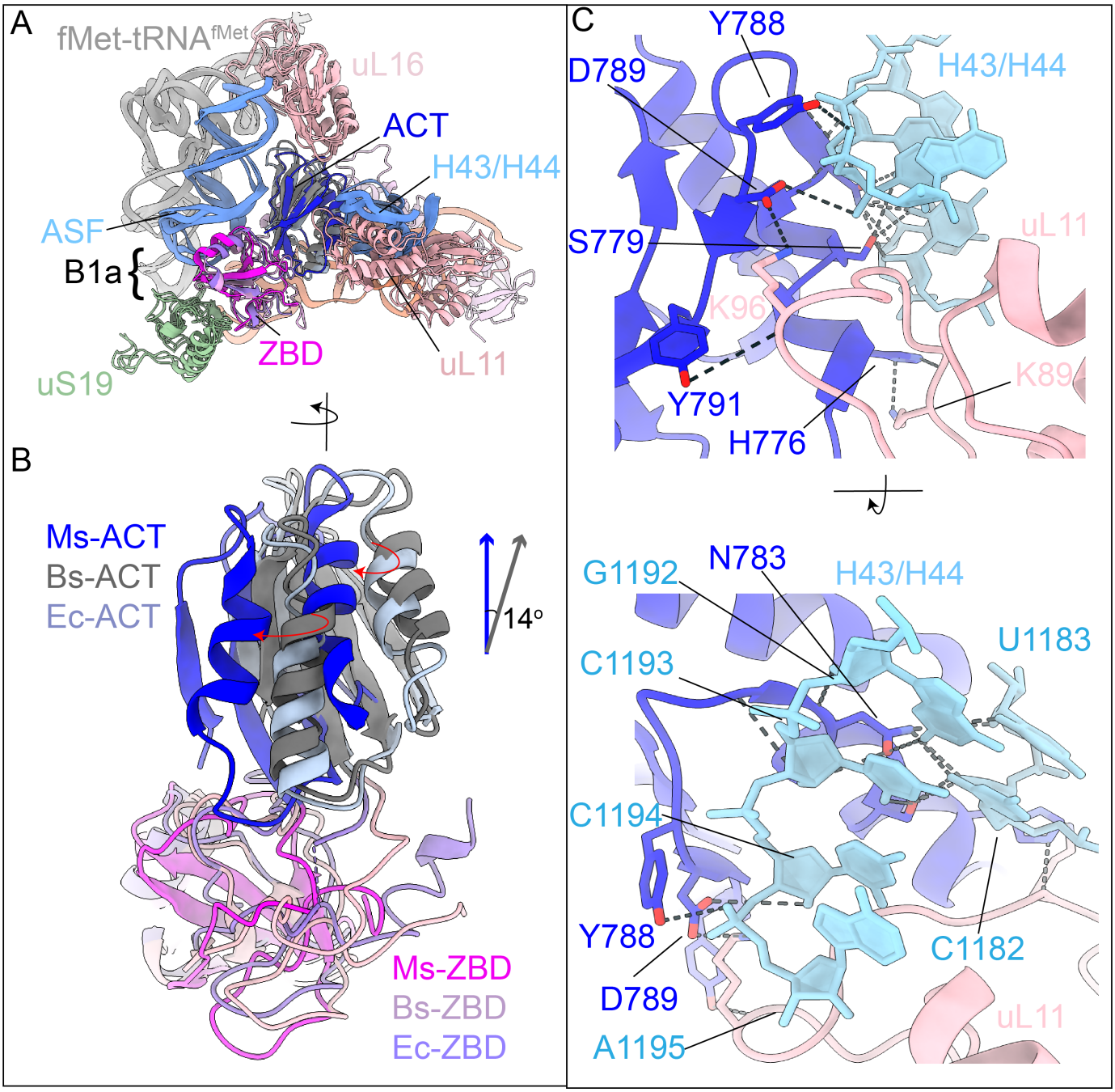
A
fMet-tRNAfMet
uL16
ACT
H43/H44
ASF
B1a
ZBD
uL11
uS19
B
Ms-ACT
Bs-ACT
Ec-ACT
14°
Ms-ZBD
Bs-ZBD
Ec-ZBD
C
Y788
D789
H43/H44
S779
uL11
K96
K89
Y791
H776
G1192
N783
H43/H44
U1183
C1193
C1194
Y788
C1182
D789
uL11
A1195

Figure 5: Conformation and interactions of the Rsh-ACT domain in a pre-elongation ribosome complex. A. Superimposition of the Rsh/Rel A interacting components from the 70S-Rsh/RelA complex structures from *M. smegmatis* (Ms) 70S-Rsh (ZBD, magenta; ACT, blue), **B.** *subtilis* (Bs) 70S-Rsh (ZBD, light pink; ACT, gray), and *E. coli* (Ec) 70S-RelA (ZBD, light purple; ACT, steel blue). Only components interacting with RelA/Rsh, L7/L12 stalk base (H43/H44 in blue), A-site finger (ASF in blue) uL16 and uL11 (light pink), the A/R tRNA (light coral) and uS19 (sea green), along with the P-site tRNA (light gray), are displayed. B. Superimposition of the C-terminal ZBD and ACT domain from Ms, Bs, and Ec (color-coded as in panel A) highlighting the rotation in Ms-ACT domain with respect to Ms-ZBD. **C.** Interactions of Ms Rsh-ACT (blue) with L11 (light pink) and the 23S rRNA helices H43/44 (light blue) are shown from two viewing directions.

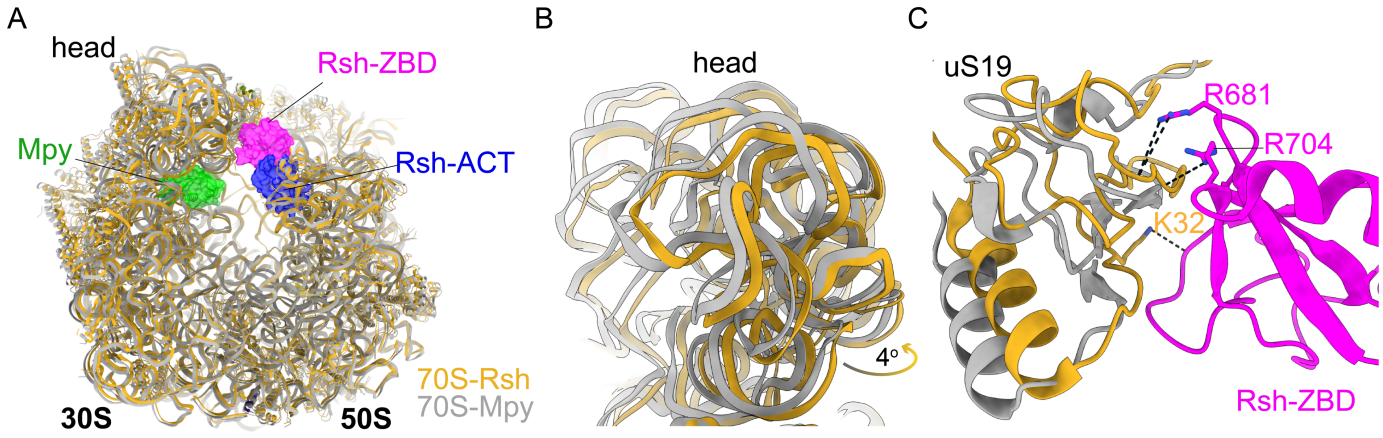

Figure 6: A structural explanation of inhibition of Rsh binding to a Mpy-bound 70S ribosome. A. Superimposition of Ms 70S-Mpy (gray, PDB ID:6DZI) and Ms 70S-Rsh (gold) structures. Rsh (ZBD, magenta; ACT, blue) and Mpy (green) are shown in the space-filled rendering. **B**. The 16S rRNAs corresponding to head domain of the 30S subunit in panel A has been enlarged to highlight the their relative position in the two functional states. **C**. The position of uS19 (gray) in the Mpy-bound state would disrupt the observed interactions between Rsh-ZBD (magenta) and uS19 (orange).

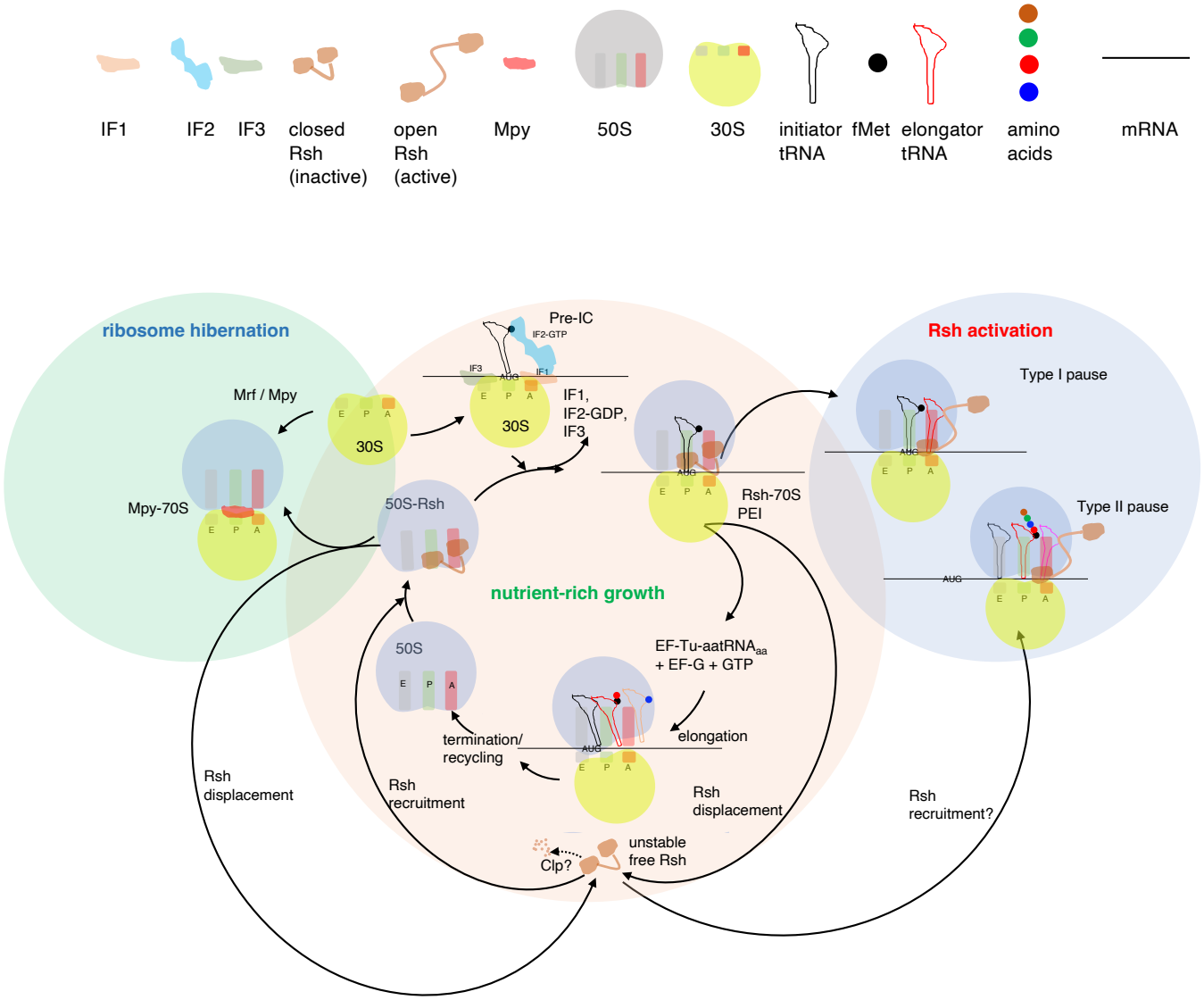

Figure 7: **Model of a dynamic interaction of Rsh with the ribosome in mycobacteria, influenced by three distinct conditions**. In a nutrient-rich condition supporting normal translation, labile Rsh predominantly remains associated with the free 50S subunit, which confers stability to the protein. Rsh-50S complex joins with a 30S pre-initiation complex (pre-IC). Following the release of initiation factors, Rsh likely remains in the pre-elongation intermediate (PEI), which in an unrotated conformation is ready to elongate upon entry of the first A- site tRNA. Rsh is likely sterically displaced during intersubunit rotation associated with the first cycle of elongation. Free Rsh associates with 50S subunit and the cycle continues until a deacylated tRNA enters the A-site at the second codon (type I pause), which will lead to activation of Rsh. Rsh could also potentially be activated if free Rsh interacts with a stalled ribosome downstream of the second codon (Type II pause), although its frequency could be limited by the efficiency of free Rsh in finding such complexes. Conditions inducing hibernating ribosomes, which appear to be less permissive to Rsh *in vivo*, would sequester ribosomes from translation cycle, thereby exposing Rsh to degradation in a Clp protease dependent manner.

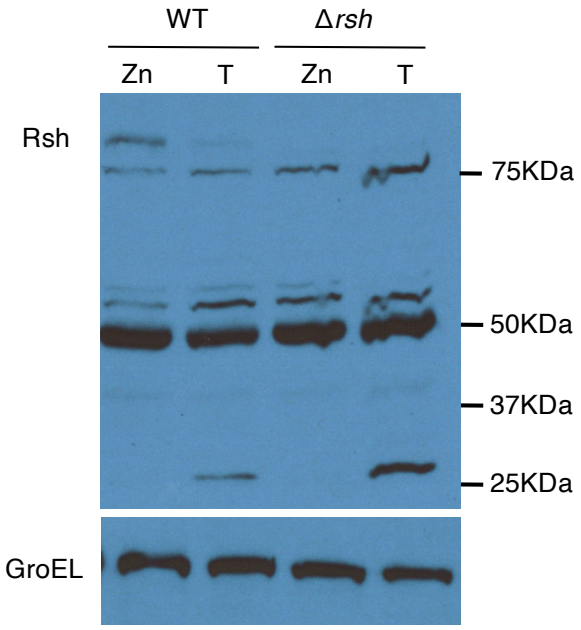

Figure S1: A full-gel immunoblot of cells lysates from WT and Δ*rsh* strains cultured in high- (1mM $ZnSO_4$; abbreviated as Zn) and low-zinc Sauton's medium (1μM TPEN; abbreviated as T) and probed with anti-Rsh antibody. Data shows lack of any Rsh-derived smaller product in the low-zinc culture. GroEL from the lysate was probed as a loading control.

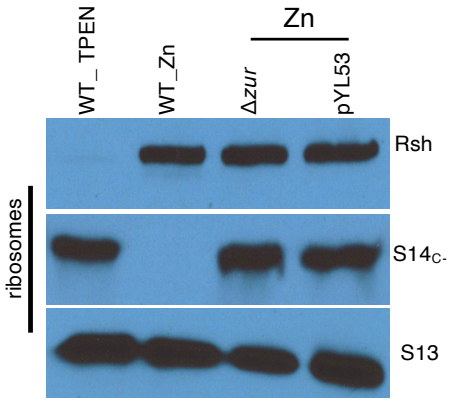

Figure S2: Effect of ribosome remodeling on Rsh-ribosome interaction. Immunoblot analysis of Rsh bound to 70S ribosomes from 96-hour old high-zinc cultures of WT *M. smegmatis* and its two recombinant strains, Δ*zur* and *pYL53,* which constitutively expressed the remodeled (C-) ribosomes. Low-zinc culture of WT was used as control.

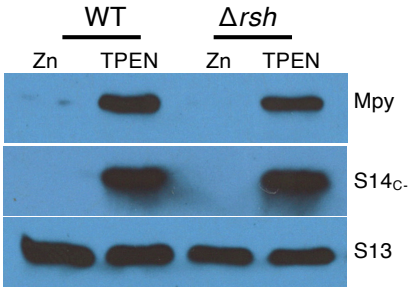

Figure S3: Levels of Mpy in the purified 70S ribosomes from high- and low-zinc cultures of WT and Δ*rsh.* $S14_{c-}$ and S13 were probed as controls as indicated.

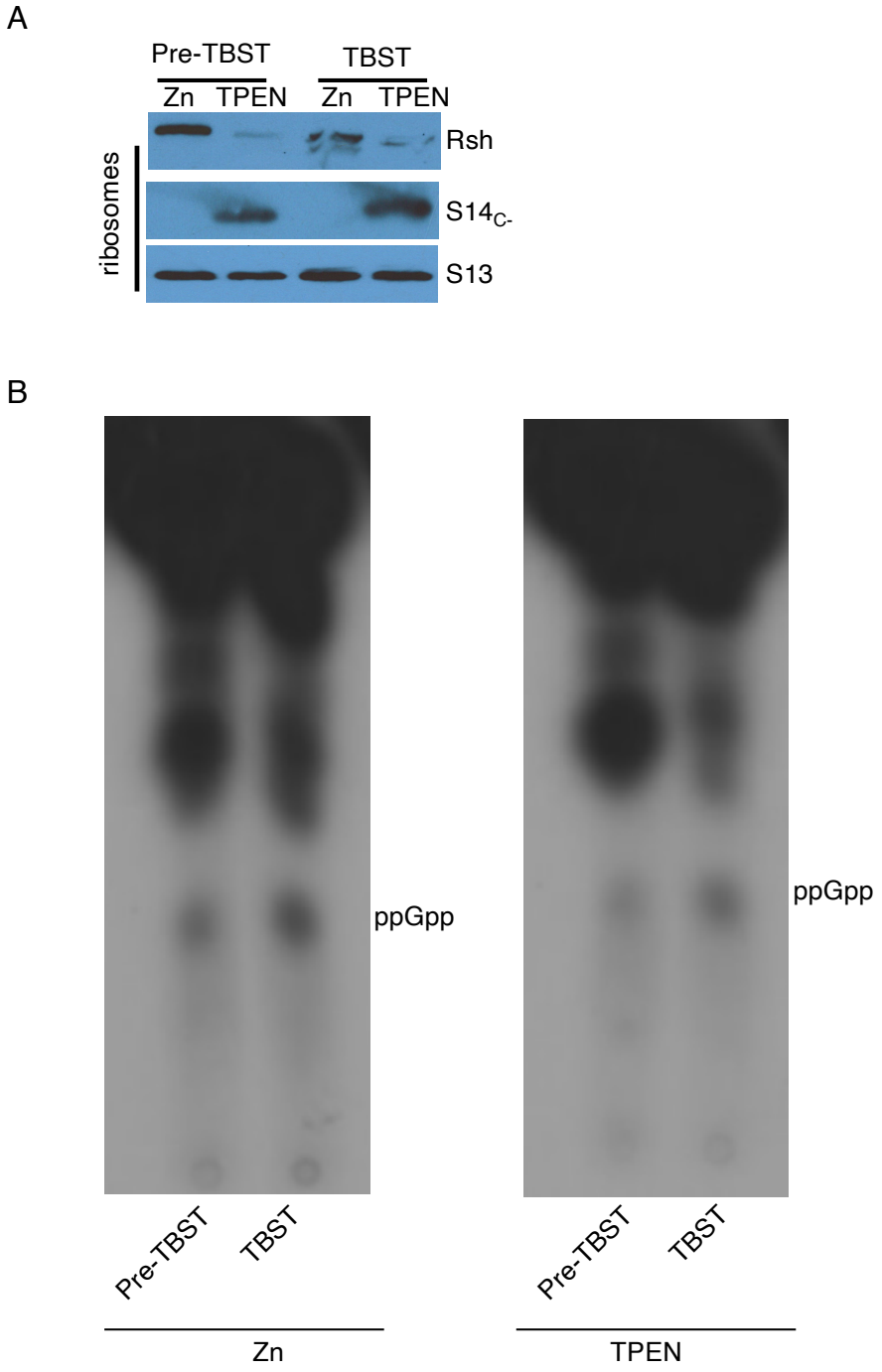

Figure S4: Level of Rsh-bound ribosomes (A) and ppGpp (B) in *M. smegmatis* before and after exposure to starvation (TBST) from high- or low-zinc culture conditions after 28 hours of growth.

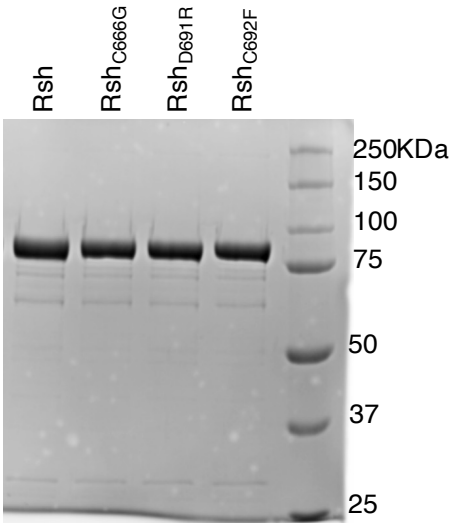

Figure S5: Purified recombinant 6XHis-tagged Rsh proteins expressed from an IPTG-inducible T7 promoter in the *E. coli* BL21 strain and visualized by SDS-PAGE and the Coomassie Blue stain. Each recombinant protein was purified from the same volume of starting cells using the same method, and equal volume of each sample was loaded on the gel.

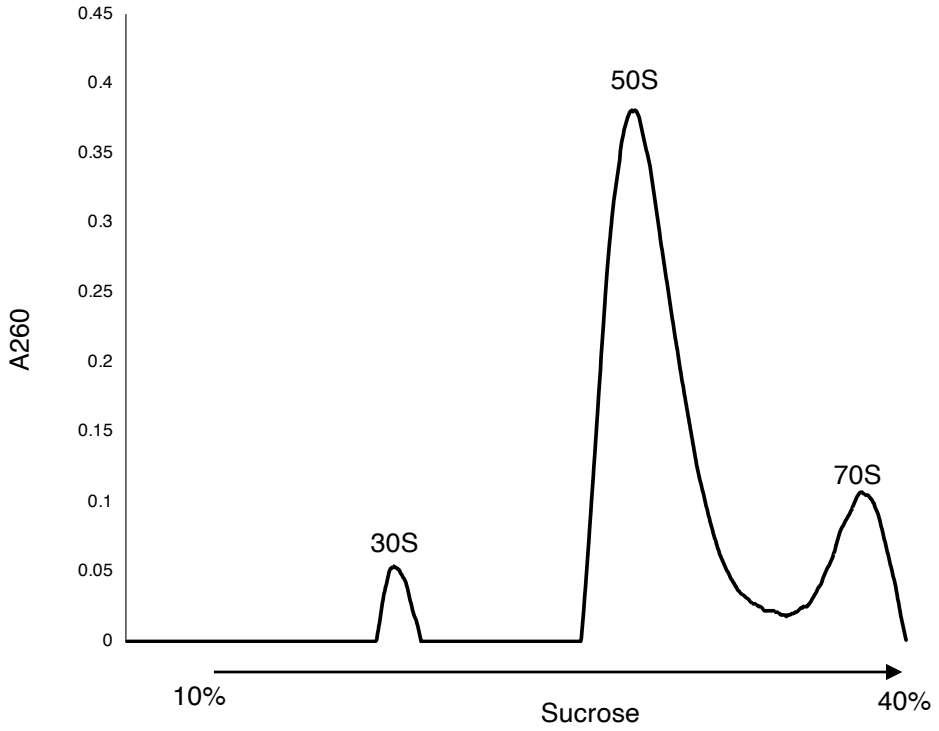

Figure S6: Sucrose density gradient profile of dissociated ribosomes used in the reconstitution experiments described in figure 4. The reconstituted ribosomal were also used for structural analysis.

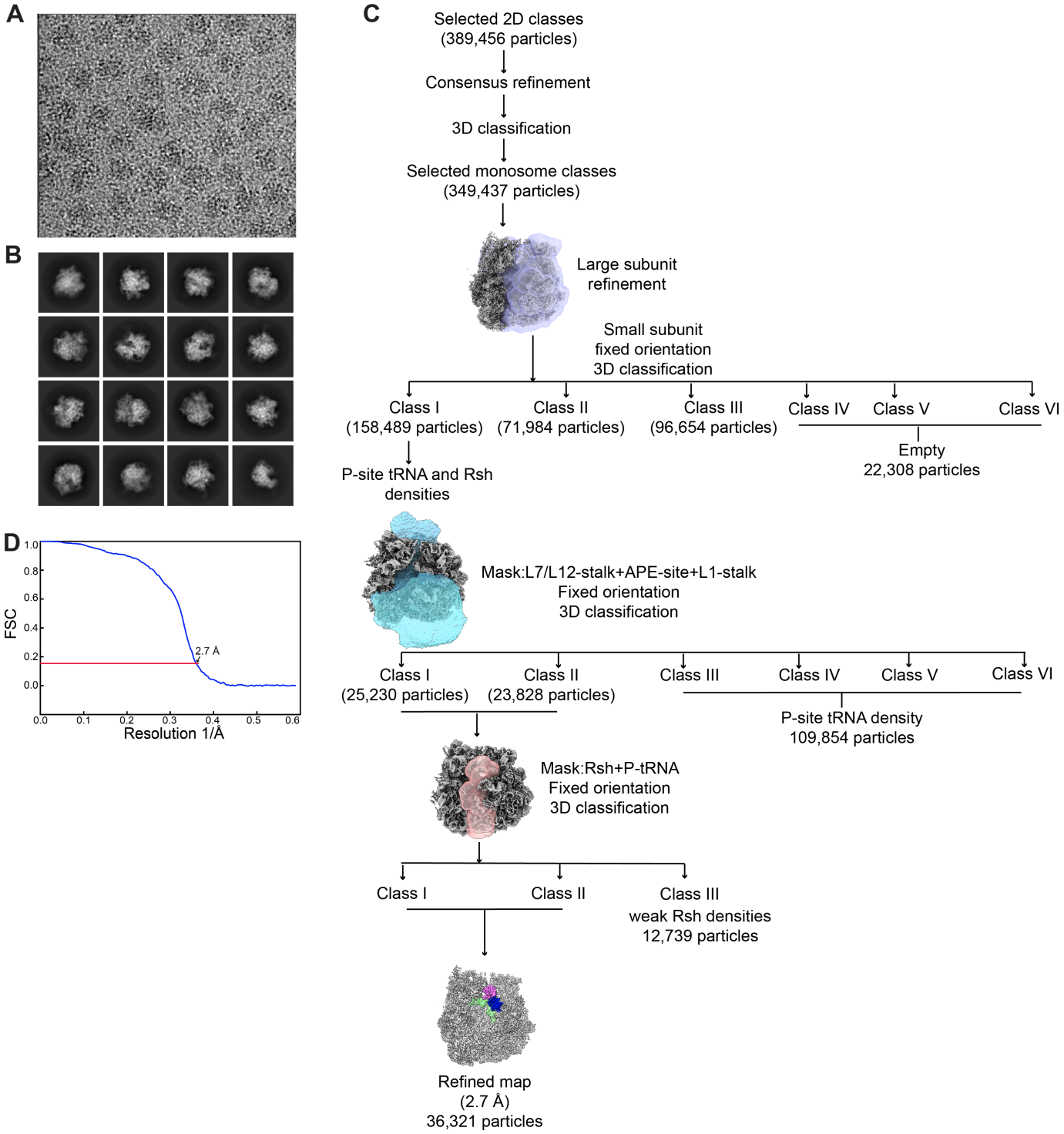

Figure S7: Image processing of *M. smegmatis* 70S-Rsh-fMet-tRNA$_i^{Met}$ complex. Image processing of *M. smegmatis* 70S-Rsh-fMet-tRNAi^{Met} complex. A. a representative micrograph from the *M. smegmatis* 70S-Rsh-fMet-tRNAi^{Met} complex dataset. **B.** Representative 2D class averages used for the 3D reconstructions. **C.** Flowchart showing the details of 3D classifications and refinements. **D.** Fourier-shell correlation (FSC) plot for the final map (36,321 particles) used in this study. Local resolution for this map is shown in figure S8.

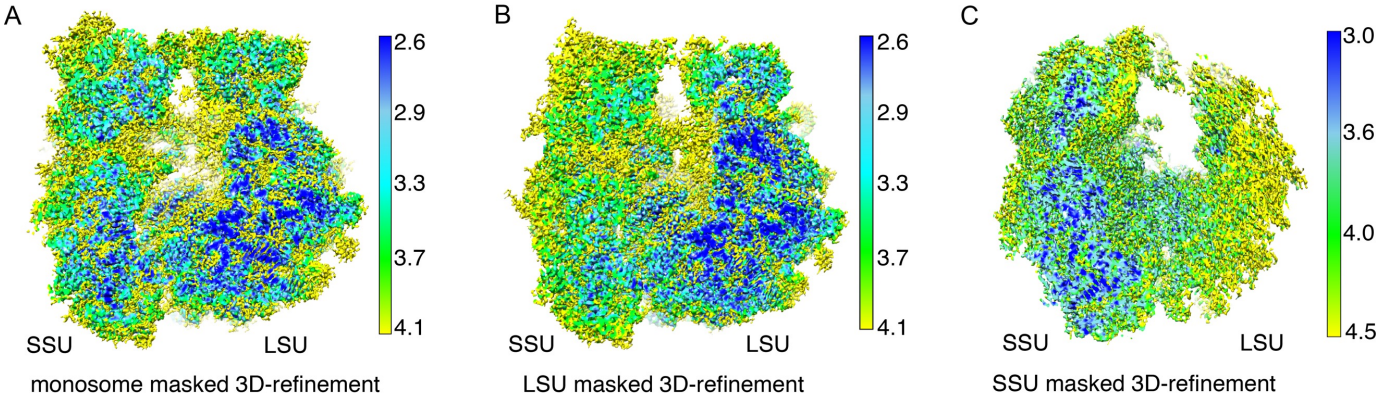

Figure S8: Local resolution of the cryo-EM map of the *M. smegmatis* 70S-Rsh-fMet-tRNAi^{Met} complex. Refined by using (A) 70S monosome, (B) 50S LSU, and (C) 30S SSU masks. In panels B and C, SSU and LSU appear to be partially disordered, as expected. A cutting plane has been applied to show the core of the ribosome in each case.

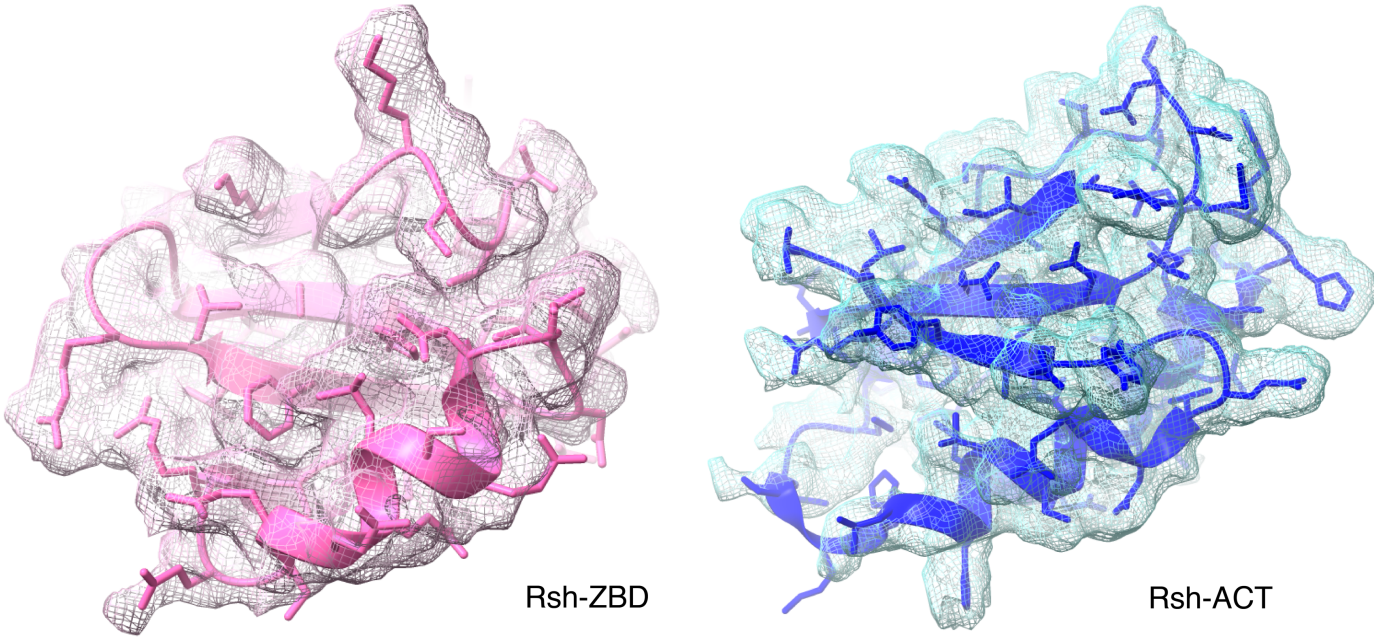

Figure S9: Modeling of the ZB- and ACT domains into corresponding cryo-EM densities. Two different density threshold values were used for modeling the two domains, as density for the main anchoring ZBD (pink) was stronger than that for the ACT domain.

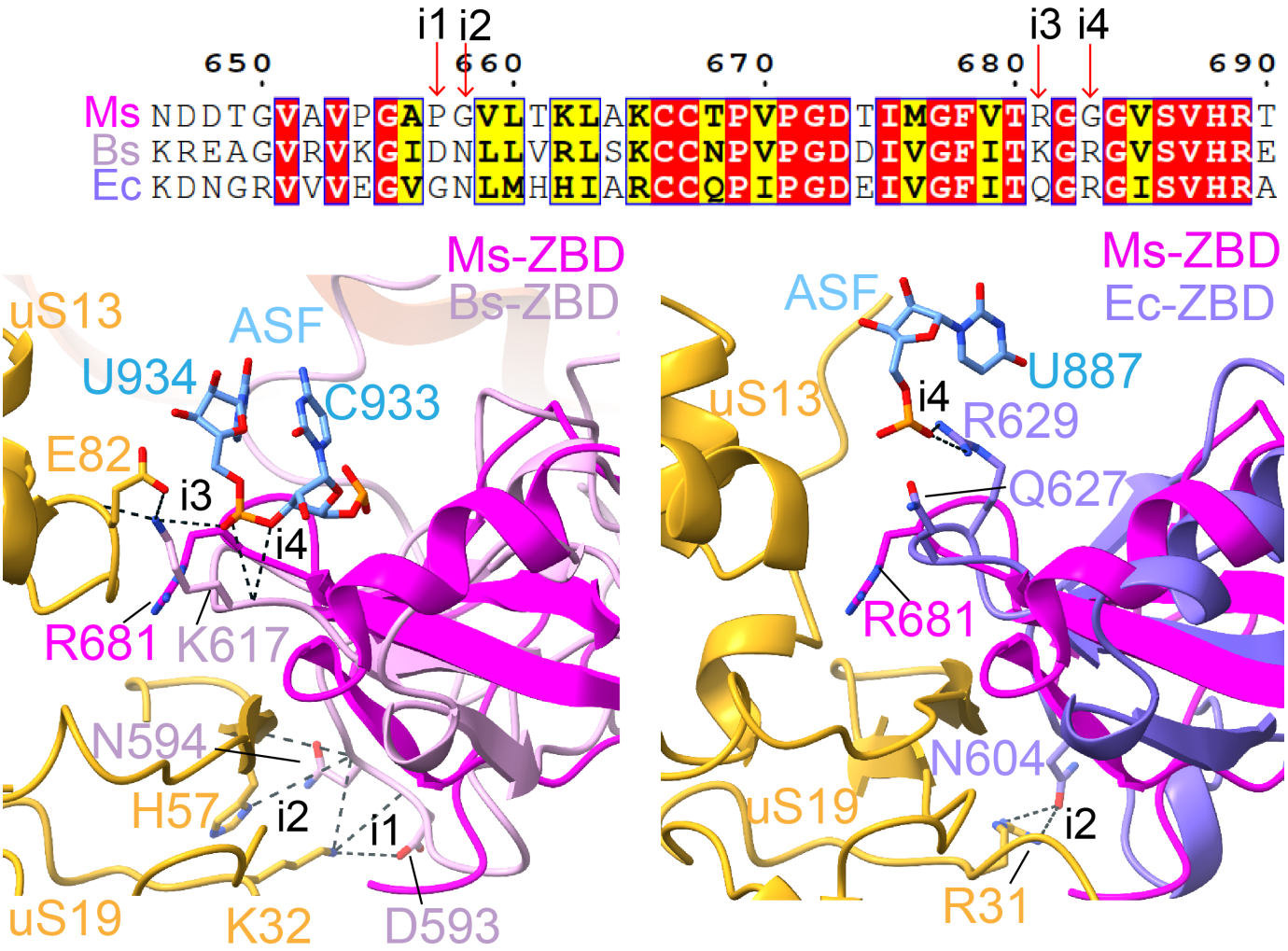

Figure S10: Species-specific differences in Rsh/RelA-ZBD interaction with uS19, uS13, and ASF. Top- Multiple sequence alignment of a short stretch in the ZBD domain of *M. smegmatis* (Ms) Rsh, *B. subtilis* (Bs) Rsh, and *E. coli* (Ec) RelA. Amino acid substitutions at four regions (indicated by red arrows) that result in species-specific differences in interactions (i1-i4) of the ZBD domain with ribosomal components. Bottom left- Superimposition of Ms 70S-Rsh (ZBD, magenta) and Bs 70S-Rsh (ZBD, light pink). Interactions of Bs-Rsh-ZBD with the ribosome that are absent in the case of Ms-Rsh-ZBD are displayed: two with uS19 (i1 and i2), one with uS13 (i3), and one with ASF (i4). Bottom right- Superimposition of Ms 70S-Rsh (ZBD, magenta) and Ec 70S-RelA (ZBD, light purple). Ec RelA-ZBD has two extra interactions with the ribosome, as compared to Ms Rsh-ZBD: One with uS19 (i2) and another with ASF (i4).

Table S1: List of plasmids and strains

Plasmids	Remarks	Reference
pJl37	P_{hsp60}-based expression vector for mycobacteria; *kan*^{r}	[1]
pMH94	L5-attp-based integrative vector for mycobacteria; *kan*^{r}	[1]
pYUB854	Cosmid vector, hygr	[1]
pTTPla	Tweety-attp-based integrative vector for mycobacteria; *kan*^{r}	[1]
pLam12	$P_{acatamidase}$-based expression vector for mycobacteria; *kan*^{r}	[1]
pJV53-SacB	Sucrose-sensitive marker SacB cloned in pJV53 @ SpeI site; *kan*^{r}	[1]
pET21b	Vectors carry an N-terminal T7-Tag sequence plus an optional C-terminal His Tag sequence, *amp*^{r}	[1]
pYL3	*kan*^{r} cassette in pMH94@EcoRV & NotI sites is replaced by *hyg*^{r} cassette from pYUB854; *hyg*^{r}	[2]
pYL40	*Msmeg_6069* internal deletion in pYL42 backbone @ SacI & XbaI, *hyg*^{r}	[1]
pYL53	MSMEG_6065-6070 cloned in pYL3 @ SacI+XbaI under a constitutive promoter (P^{const}): mutant variant of $P^{zur\text{-}box}$, *hyg*^{r}	[1]
pYL155	C-terminally FLAG-tagged *mrf* with P^{zurbox} cloned in pTTPla @ SacI & XbaI sites; *kan*^{r}	[1]
pYL181	C-terminally FLAG-tagged *mrf* with P^{zurbox} cloned in pYL180 @ SacI & XbaI sites; *apr*^{r}	[1]
pYL206	L5-attp-based integrative vector carrying tet-inducible dCas9 and gRNA complementary to Clpp1; *kan*^{r}	[1]
pYL222	*Msmeg_6069* with all six his/cys mutations (H to A, C to A) and Flag tag at C-terminal and $p^{zur\text{-}box}$ cloned in plam12 @ XbaI & HindIII sites; *kan*^{r}	This Study
pYL236	*MSMEG_2965* (T518A) + 500 bp UPS cloned in pMH94 @ KpnI & XbaI; *kan*^{r}	This Study
pYL238	*MSMEG_2965* + 500 bp UPS cloned in pMH94 @ KpnI & XbaI; *kan*^{r}	This Study
pYL239	*MSMEG_2965* (S519A) + 500 bp UPS cloned in pMH94 @ KpnI & XbaI; *kan*^{r}	This Study
pYL240	*MSMEG_2965* with C666G mutation + 500 bp UPS cloned in pMH94 @ KpnI & XbaI; *kan*^{r}	This Study
pYL241	*MSMEG_2965 with D691R mutation* + 500 bp UPS cloned in pMH94 @ KpnI & XbaI; *kan*^{r}	This Study
pYL242	*MSMEG_2965 with C692F mutation* + 500 bp UPS cloned in pMH94 @ KpnI & XbaI; *kan*^{r}	This study
pYL243	*MSMEG_2965* with N-terminal His-tag cloned in pET21b @ NdeI & HindIII; *amp*^{r}	This study
pYL246	*MSMEG_2965* (C666G) with N-terminal His-tag cloned in pET21a @ NdeI & HindIII; *amp*^{r}	This study
pYL247	*MSMEG_2965* (D691R) with N-terminal His-tag cloned in pET21a @ NdeI & HindIII; *amp*^{r}	This study
pYL248	*MSMEG_2965* (C692F) with N-terminal His-tag cloned in pET21a @ NdeI & HindIII; *amp*^{r}	This study
pYL259	*MSMEG_2965* + 500 bp UPS cloned in pYL3 @ KpnI & XbaI; *hyg*^{r}	This study
pYL260	*MSMEG_2965* (C666G)+ 500 bp UPS cloned in pYL3 @ KpnI & XbaI; *hyg*^{r}	This study
pYL261	*MSMEG_2965* (D691R)+ 500 bp UPS cloned in pYL3 @ KpnI & XbaI; *hyg*^{r}	This study
pYL262	*MSMEG_2965* (C692F)+ 500 bp UPS cloned in pYL3 @ KpnI & XbaI; *hyg*^{r}	This study
Strains	**Remarks**	**Reference**
mc^2*155 (WT)*	High-Frequency Transformation strain of *M. smegmatis* as parent wild-type	[2]
Δmsm$_{c-}$	Unmarked Δ*Msmeg_6065-6070* in mc^{2}155	[2]
Δ*mrf (YL1)*	Unmarked Δ*c-* operon harboring pYL40; *hyg*^{r}	[1]
Δ*mrf*comp (YL2)	Unmarked Δ*c-* operon harboring pYL40 and pYL155; *hyg*^{r}, *kan*^{r}	[1]
Δ*mpy* (YL3)	Unmarked Δ*Msmeg_1878* in mc^{2}155	[2]
Δ*mpy*/Δ*mrf* (YL4)	Unmarked Δ*Msmeg_6065-6070*/Δ*Msmeg_1878* harboring pYL40; *zeo*^{r}, *hyg*^{r}	[1]

Δ*zur* (YL5)	Unmarked Δ*Msmeg_4487* in mc^{2}155	[2]
Δ*zur*/Δmrf (YL6)	Unmarked Δ*Msmeg_6065-6070* /Δ*zur* harboring pYL40; *hyg*^{r}	[1]
YL9	Δ*zur* harboring pYL181 and pYL206; *apr*^{r}, *kan*^{r}	[1]
Δ*rsh*	Δ*Msmeg_2965* in mc^{2}155, *zeo*^{r}	This Study
mc^{2}7000	*M. tuberculosis* H37Rv:*ΔRD1*:*ΔpanCD* as parent wild-type	[2]
Δmpy$_{mtb}$	*ΔRv_3241c* in mc^{2}7000 or Mtb(Erd)	[1]
Δmrf$_{mtb}$	*ΔRv_0106* in mc^{2}7000	[1]
*Δmrf$_{mtb}$*comp	*ΔRv_0106* harboring pYL149 in mc^{2}7000	[1]

1. Li Y, Corro JH, Palmer CD, Ojha AK: **Progression from remodeling to hibernation of ribosomes in zinc-starved mycobacteria**. *Proceedings of the National Academy of Sciences of the United States of America* 2020, **117**(32):19528-19537.
2. Li Y, Sharma MR, Koripella RK, Yang Y, Kaushal PS, Lin Q, Wade JT, Gray TA, Derbyshire KM, Agrawal RK *et al*: **Zinc depletion induces ribosome hibernation in mycobacteria**. *Proc Natl Acad Sci U S A* 2018, **115**(32):8191-8196.

Table S2: Synthetic oligonucleotides and IF2 sequences

Name	Sequence	Used in:
His1-R	GGTGCGGACGACGACAGCGCCGTCGAAGGTGGCGCTGACGAGCAGGGT	pYL222
His1-F	ACCCTGCTCGTCAGCGCCACCTTCGACGGCGCTGTCGTCGTCCGCACC	
His2-R	GGCCGAGACGGCTCCGGCCACCAGCTCAAGTAC	
His2-F	GTACTTGAGCTGGTGGCCGGAGCCGTCTCGGCC	
His3-R	CACGTCGGCGCGCCGGGCCAGACGGCGAAGCAGGAT	
His3-F	ATCCTGCTTCGCCGTCTGGCCCGGCGCGCCGACGTG	
p6069-CXXCR	ATCGTCACGCACGGTGGCCGAGACGGCTCCGTGCACCAGCTC	
p6069-CXXCF	GAGCTGGTGCACGGAGCCGTCTCGGCCACCGTGCGTGACGAT	
Pzurbox 6069-XF	CGCGCCGTTCGTCTAGACGCTGCACCAGTTCTCGCC	
p6069-FLAGHR	GGCCGGAAGCTTTCACTTATCGTCGTCATCCTTGTAATCCGATTGCTCTCCTGT	
pRelAMS-up500KpnIF	CTTCCCCGAACCGGTACCCCAGTTCAAGGACCTCAC	pYL236,238, 239,240,241, 242,256,259, 260,261,262
pRelAMS-XbaIR	CGCCGAACCTCTAGATTAGGCCGCGCTGGTGACGCG	
RelAC666G-F	ACCAAGCTGGCCAAGGGCTGCACCCCGGTGCCG	pYL240,246, 260
RelAC666G-R	CGGCACCGGGGTGCAGCCCTTGGCCAGCTTGGT	
RelAD691R-F	AGCGTGCACCGCACCCGTTGCACCAACGCCGAG	pYL241,247, 261
RelAD691R-R	CTCGGCGTTGGTGCAACGGGTGCGGTGCACGCT	
RelAC692F-F	GTGCACCGCACCGACTTCACCAACGCCGAGTCG	pYL242,248, 262
RelAC692F-R	CGACTCGGCGTTGGTGAAGTCGGTGCGGTGCAC	
prelA-NdeIHISF	TGACACATATGCACCACCACCACCACCACGTCGACGAGCCAGGCAAG	pYL243,246, 247,248
prel-HindIIItgaR	CGCCGAACCGCTAAGCTTTCAGGCCGCGCTGGTGACGCG	

> Sequence of codon optimized synthetic IF2:
ATACGAGAACCATatgCACCACCACCACCACCACCAGGCACCGGTCGTGGGAGGGGTAAGACTTCCTCA
CGGTAACGGCGAGACGATCCGTCTGGCACGCGGCGCTTCATTATCAGATTTTGCTGAAAAGATAAATG
CGAATCCGGCTTCACTTGTGCAGGCATTGTTCAATCTTGGAGAAATGGTTACTGCCACGCAAAGTGTCG
GTGATGAAACACTTGAGCTGTTAGGGTCGGAGATGAATTACAATGTACAGGTCGTATCACCAGAAGACG
AGGACCGTGAATTGCTTGAAAGCTTTGATTTAACCTACGGCGAAGACGCGGGTGACGAGGAGGACTTA
GAGGTGCGTCCACCCGTTGTAACCGTTATGGGCCATGTCGATCATGGTAAGACTAGACTTCTGGACAC
AATCCGGAAGGCAAATGTGAGAGAGGGCGAGGCCGGCGGTATAACGCAGCACATCGGGGCCTATCAG
GTTGAGGTTGATTTGGACGGGACGGTGCGTCCCATAACTTTTATTGATACTCCCGGTCACGAGGCCTTT
ACCGCAATGCGTGCCAGAGGTGCCAAGGCTACAGATATTGCTATTTTAGTGGTAGCCGCGGATGATGG
CGTGATGCCTCAAACGGTTGAAGCGATTAACCACGCACAGGCCGCGGACGTTCCGATAGTGGTAGCA
GTCAACAAAATTGATAAGGAAGGAGCGGACCCCGCTAAAATTCGTGGGCAGTTAACAGAATATGGATTA
ATACCGGAAGAGTATGGCGGAGACACCATGTTTGTAGATATCAGTGCGAAACAGGGAACAAATATTGAA
GCATTATTAGAAGCAGTGATTCTTACCGCAGACGCCTCTTTAGATTTGCGTGCAAACCCCGATATGGAA
GCTCAGGGAGTCGCTATAGAAGCCCATCTTGACAGAGGTCGGGGTCCTGTTGCTACTGTATTGATACA

GCGCGGCACCCTTCGGGTTGGTGATTCCGTTGTTGCGGGTGACGCTTATGGGAGAGTCCGGAGAATG
ATCGATGAACATGGAGAGGACGTCGAAGAAGCATTGCCGTCTCGGCCGGTCCAGGTAGTTGGTTTCAC
CTCGGTACCCGGCGCTGGGGACAATTTTTTAGTTGTAGATGAAGATCGGATCGCGCGTCAAATCGCGG
ATCGCCGGTCAGCGCGTAAACGGAACGCCCTTGCTGCACGTAGTCGCAAACGGATCAGCTTGGAGGA
CTTAGACTCCGCCCTTAAAGAGACGTCGCAATTAAACCTTATATTAAAAGGAGACAACGCGGGGACAGT
TGAAGCACTGGAAGAGGCCTTAATGGGAATCCAGGTGGACGACGAGGTAGAACTGCGCGTCATCGAC
CGCGGTGTCGGAGGCGTCACAGAAACGAATGTAAACTTAGCAAGTGCCTCGGACGCGATTATCATTGG
TTTTAACGTCCGGGCTGAAGGAAAGGCGACTGAATTGGCTAATAGAGAAGGAGTTGAAATACGCTATTA
TTCTGTAATCTACCAGGCGATTGATGAAATTGAAGCAGCACTTAAAGGAATGCTGAAGCCTGTATACGA
AGAGAAGGAGCTTGGGCGTGCAGAAATACGTGCCATCTTCCGCAGTTCTAAGGTGGGCAATATAGCTG
GCTGCCTTGTCACATCAGGAATAATGCGCCGCAACGCTAAGGCCCGTTTATTAAGAGACAATGTAGTAG
TTGCACAGAATTTGACGGTAAGTAGTTTAAGACGCGAAAAGGATGACGTAACGGAAGTTCGTGATGGTT
ACGAGTGCGGACTGACCTTAACCTATAATGACATCAAAGAAGGTGACGTAATTGAGACTTATGAATTAG
TTGAAAAAGCGCGTACTtgaCTCGAGTGGCCGATCC

Table. S3 Data collection, Refinement and Model Validation parameters.

Description	**70S-Rsh-fMet-tRNA$_i^{Met}$ complex**
Data collection	
Microscope	FEI Titan Krios
Voltage (kV)	300
Pixel size (Å)	0.846
Defocus range (μm)	-1.50 to -2.50
Average e^- dose per image (e^-/ Å^2)	66.59
Particles (initial)	1,928,609
Particles (final)	36,321
FSC-threshold	0.143
Resolution (Å)	2.7
Map-sharpening B factor (Å^2) overall	-44.3
Refinement	
RMS deviations	
Bonds (Å)	0.007
Angles (^{o})	0.923
MolProbity score	1.80
Clash score	6.43
Rotamer outliers (%)	0.61
Ramachandran plot	
Outliers (%)	0.16
Allowed (%)	6.72
Favored (%)	93.12
RNA	
Correct sugar puckers (%)	99.4
Angle outliers (%)	0.02
Bond outliers (%)	0.00
Good backbone conformations (%)	75.9
Model composition	
RNA bases	4843
Protein residues	11,068